

ABSTRACT

WENWEN, ZHANG. Wetting Behavior of Liquid Aerosols on Spider Webs and Creation of Liquid Aerosol Barriers. (Under the direction of Dr. Stephen Michielsen).

Liquid aerosols occur widely in our environment, including clouds, haze, and air pollution, such as smog and smoke. Liquid aerosols that are composed of harmful chemicals or biochemical ingredients are extremely harmful to human health. When biochemical components participate, it is very hard to block them with normal superhydrophobic textile droplet barriers because of their small volume. Spider webs, which can collect moisture from high relative humidity environments and form larger water droplets, have been found that have spindle knot structures. After their discovery, spindle knots have been assumed as the key reason to move the tiny droplets directionally and spontaneously. However, these studies did not provide solid understanding about why it happens. The primary targets of this study are to understand the fundamental science behind the wetting behavior of liquid aerosols and to design and produce a textile barrier, which is “super-aerosol-phobic”. In this study, the fundamentals of directional motion of water droplets on spindle knots have been investigated using both theoretical and experimental approaches based on Gibbs free energy, capillarity and Laplace pressure. Meanwhile, the structure of aerosol liquid barrier has been optimized and initial materials created.

© Copyright 2014 Wenwen Zhang

All Rights Reserved

Wetting Behavior of Liquid Aerosols on Spider Webs and
Creation of Liquid Aerosol Barriers.

by
Wenwen Zhang

A dissertation submitted to the Graduate Faculty of
North Carolina State University
in partial fulfillment of the
requirements for the degree of
Doctor of Philosophy

Fiber and Polymer Science

Raleigh, North Carolina

2015

APPROVED BY:

Dr. Stephen Michielsen
Committee Chair

Dr. David Hinks

Dr. Melissa A. Pasquinelli

Dr. Tiegang Fang

DEDICATION

To my family and my advisors.

BIOGRAPHY

The author was born in Weifang, Shandong province, China. She received the Shanghai Excellent Graduate Award together with Bachelor of Engineering in Textile Engineering (Textile Testing and Commerce) from Donghua University in July 2010. In December, 2012, she received the Master of Science degree in Textile Engineering from College of Textiles at North Carolina State University. In August 2012, she started her Doctor of Philosophy degree in Fiber and Polymer Science from College of Textiles at North Carolina State University.

ACKNOWLEDGMENTS

I appreciate Dr. Michielsen's guidance throughout my PhD and life in the US. He is full of patience and responsibility to me. In my PhD study, he guided me at every moment I needed suggestions. He trusted my ideas proposed to him each time and encouraged me to explore the answers. More importantly, he offered me a lot of help in my life whenever I needed directions. Choosing him as my advisor for my master and PhD degrees is the best decision I made.

I want to express my special appreciation to Dr. Hoon Joo Lee, who had been my co-chair for the first one and half years of my PhD study. She is very helpful in helping me to build efficient communication skills and formal document writing ability. Especially, I would like to appreciate her sincerity to me. I will always remember her corrections in emails, her encouragement in her office, and her suggestions during biweekly group meeting.

I also acknowledge the members of my committee Dr. David Hinks, Dr. Melissa A. Pasquinelli, and Dr. Tiegang Fang for their interest and help. I would like to thank Judy D Elson, Vicki Stocksdales and Amanda Holbrook for their help throughout my research. I would also like to thank the College of Textiles' staff, who helped me during my research. I wish to express my appreciation to U.S. Army Natick Soldier RD&E Center and College of Textile for funding this research.

I thank my parents, brother and sister-in-law for their endless love and support throughout my life. I thank my nephew and niece for the joy they brought to me through my study. I thank my husband for his tolerance, patience, silent support, and peaceful joy in my study. I thank my friends and colleagues for endless support throughout my study.

TABLE OF CONTENTS

LIST OF TABLES	viii
LIST OF FIGURES	ix
1. INTRODUCTION	1
2. LITERATURE REVIEW	3
2.1. Liquid Interface	3
2.1.1. Surface Tension of a Liquid.....	3
2.1.2. Laplace Pressure	6
2.1.3. Thermodynamics of Liquid Interface	8
2.1.4. Orientation at the Interface	10
2.2. Solid Interface	11
2.2.1. Surface Tension of Solids	11
2.2.2. Theoretical Estimates of Surface Energies	12
2.2.3. Surface Characterization Techniques	12
2.2.4. Surface Modifications	13
2.3. Solid-Liquid Interaction	14
2.3.1. Introduction.....	14
2.3.2. Contact angle	15
2.3.3. Capillarity	18
2.3.4. Plateau-Rayleigh Instability.....	21
2.4. Droplets	22
2.4.1. Introduction.....	22
2.4.2. Interaction between droplets.....	22
2.4.3. Precursor of droplets	27
2.4.4. Droplet on a cylindrical fiber	30
2.4.5. Droplets on conical fiber.....	32
2.4.6. Droplets on spindle knots.....	35
2.5. Summary of literature reviews	40
3. EXPERIMENT	42
3.1. Materials.....	42

3.2.	Equipment	42
3.2.1.	Droplet Deposition tools.....	43
3.2.2.	Contact Angle Measurement tools	44
3.2.3.	Evaporation Suppression Chamber	46
3.2.4.	Microliter Droplet Observation System	47
3.2.5.	Picoliter Droplet Observation System	48
3.3.	Structure Formation.....	50
3.3.1.	Formation of flat smooth surface.....	50
3.3.2.	Formation of fibers	51
3.3.3.	Formation of Cones	51
3.3.4.	Formation of Spindle Knot Fiber.....	51
3.4.	Surface Modification.....	52
3.5.	Wetting Behavior of Droplet on Flat Surface	53
3.5.1.	Microliter droplet on flat surface.....	53
3.5.2.	Picoliter droplet on flat surface	53
3.6.	Droplet Profile.....	54
3.6.1.	Microliter Droplet on cylindrical fiber	54
3.6.2.	Picoliter Droplet on cylindrical fiber.....	55
3.7.	Droplet Coalescence.....	55
3.7.1.	Microliter Droplet on yarns	55
3.7.2.	Picoliter Droplet on grooved Fiber	55
3.8.	Droplet Motion.....	56
3.8.1.	Microliter shape droplet on spindle knot.....	56
3.8.2.	Picoliter shape droplet on spindle knot.....	57
3.8.3.	Clamshell Shape Droplet on Cone.....	58
4.	RESULTS AND DISCUSSION.....	59
4.1.	Droplet on Flat Surface	59
4.1.1.	Microliter Droplet on Flat Surface	59
4.1.2.	Picoliter Droplet on Flat Surface	61
4.2.	Droplet on Single Fiber	61

4.2.1.	Droplet on Cylindrical Fiber.....	62
4.2.1.1.	Barrel Shaped Droplet on Cylindrical Fiber	63
4.2.1.2.	Clamshell Shaped Droplet on Cylindrical Fiber	63
4.2.1.3.	Droplet Growth on Cylindrical Fiber.....	63
4.2.2.	Droplet on Conical Fiber	68
4.2.2.1.	Barrel Shaped on Conical Fiber	68
4.2.2.2.	Clamshell Shaped droplet on Conical Fiber	68
4.2.2.3.	Droplet Growth on Conical Fiber	73
4.2.3.	Droplet on Spindle Knot Fiber	74
4.2.3.1.	Barrel Shape on Single Spindle Knot	74
4.2.3.2.	Clamshell Shaped Droplet on Single Spindle Knot.....	82
4.2.3.3.	Small Droplet Collection on Connected Spindle Knot Fiber.....	84
4.3.	Droplet on Multifilament Yarn	87
4.3.1.	Capillarity on Grooved Fibers	87
4.3.2.	Droplet Coalescence on Multifilament Yarn.....	90
4.3.3.	Droplet Coalescence on Spider Silk	96
4.4.	Design of the Highly Efficient Aerosol Barrier	99
4.4.1.	Design of the Yarn Structure	99
4.4.2.	Design of the Fabric Structure.....	101
5.	CONCLUSION	103
6.	FUTURE STUDY	105
	REFERENCES	106

LIST OF TABLES

Table 3-1. The surface tension of liquids used.	53
Table 3-2. The parameters of picoliter droplet applicator.	53
Table 3-3. The parameters of high speed camera.	54
Table 3-4. The label indicating the spindle knot used and the shape parameters of the spindle knots.....	57
Table 4-1. Contact angles of different droplets on flat surfaces.	60
Table 4-2. The final location of the liquid drops on the spindle knots from the theoretical calculations and from experiments	76
Table 4-3 The comparison between theory and experiment in terms of number of groups at each equilibrium location.....	79
Table 4-4 Experimental Drop Parameters for Several Coalescing Water Droplet Pairs	93

LIST OF FIGURES

Figure 2-1. The scheme of surface tension.	5
Figure 2-2. The condition for mechanical equilibrium for an arbitrarily curved surface. ¹⁸	8
Figure 2-3. The two possible chemical orientations at ethanol liquid interface.	11
Figure 2-4. The scheme of contact angle.	15
Figure 2-5. Liquid droplet on a rough surface: (a) Wenzel model, and (b) Cassie-Baxter model.....	17
Figure 2-6. Capillary rise (capillary much magnified in relation to dish) ¹⁸	18
Figure 2-7. The pressure driven flow model used by Hagen Poiseulle Law.	20
Figure 2-8. A uniform coating on a fiber experiences small fluctuations in its radius. To minimize free energy, this disturbance grows into nearly equally spaced drops. ⁵²	22
Figure 2-9. Microfluidic channels used for droplet merging process. ⁵⁴	23
Figure 2-10. Schematic side and top view of electrowetting-based mixing actuator.	24
Figure 2-11. The scheme of mechanism of electrowetting array.....	25
Figure 2-12. Static contact angles of the wettability gradient surface and initial positions of the moving droplet (I) and stationary droplet (II)	26
Figure 2-13. Precursor film of a spreading droplet (M-CL: motion of contact line).....	27
Figure 2-14. Precursor film length against the non-dimensional Capillary number.....	28
Figure 2-15. Image of simulation of polymer droplets on surfaces.	29
Figure 2-16. Ionic beads and liquid precursor film.....	30
Figure 2-17. The droplet prolife on a cylindrical surface.	31
Figure 2-18. The procedure of Surface Evolver for barrel shape and clamshell droplet.	32
Figure 2-19. The schemes of the two possible cases in droplet wetting ⁶	34
Figure 2-20. The spontaneously motion of clamshell droplet on cone ⁵	35
Figure 2-21. The structure of cribellate spider silk. ⁴	36
Figure 2-22. The profile of spindle knot built on fiber.	37
Figure 2-23. The procedure of making manmade spider silk with spindle knots.....	38
Figure 2-24. The structure of artificial spider silk and water collection. ⁴	39
Figure 3-1. The mist mode generated by perfume sprayer and droplet mode produced by picoliter applicator are shown.	43
Figure 3-2. The contact angle measurement apparatus.....	45
Figure 3-3. The contact angle measurement method.	46
Figure 3-4. The three views of the evaporation suppression chamber: end, side, and top (The black is aluminum, the white color is the transparent glass, copper wire is applied to fasten the glass and the aluminum part together, and grey is a transparent polyester film).....	47
Figure 3-5. The improved measurement system showing the video-microscope in the foreground and the recorded image in the background. The chamber is in the middle.....	48

Figure 3-6. The apparatus for observation of picoliter droplets using a high-speed video camera.	49
Figure 3-7. The details of the fiber sample stabilization system.	50
Figure 3-8. The production of spindle knot fiber through UV photo polymerization.	52
Figure 4-1. The droplet profile on different flat surfaces.	59
Figure 4-2. The dodecane droplet growth on PMMA flat surface.	61
Figure 4-3. Barrel shape and clam-shell shape profiles on PP fiber.	62
Figure 4-4. Water growth on PMMA smooth fiber under droplet mode.	64
Figure 4-5. Water droplet on PMMA smooth fiber under mist mode.	65
Figure 4-6. Dodecane on smooth PMMA fiber under droplet mode.	66
Figure 4-7. Dodecane on smooth PMMA fiber under mist mode.	66
Figure 4-8. A schematic of the growth process droplets.	67
Figure 4-9. Comparison of the shape of the 1 μL water droplet based on simulation and experiment.	69
Figure 4-10. Comparison of the shape of the 1 μL Glycerol droplet based on simulation and experiment.	70
Figure 4-11. Comparison of the shape of the 1 μL Kaydol droplet based on simulation and experiment.	71
Figure 4-12. 0.1 μL water droplets on indium cone (cone angle is 14° and length of the widest part is $1214 \mu\text{m}$).	72
Figure 4-13. The relationship between cone and spindle knots.	74
Figure 4-14. Illustration of parameters and boundary conditions in case I and case II (D is the fiber diameter, W is the maximum width of the spindle knots, α and θ are the half cone angle and contact of the droplet on spindle knot surface).	75
Figure 4-15. A water clamshell droplet on a spindle knot fiber (0.1-water-P-21).	79
Figure 4-16. The theoretical study of the Gibbs energy trend and the experimental verification (0.1-Dodecane-P-20).	80
Figure 4-17. The theory study of the Gibbs energy trend and the experimental verification (0.1-dodecane-F-19).	81
Figure 4-18. Dodecane droplet on PMMA single fiber.	82
Figure 4-19. Water clamshell droplet on PMMA single spindle knot fiber (fiber diameter is $450 \mu\text{m}$).	83
Figure 4-20. Water clamshell droplet on PMMA single spindle knot (fiber diameter $30 \mu\text{m}$).	83
Figure 4-21. Dodecane droplet collection on connected spindle knots under mist mode.	84
Figure 4-22. Dodecane droplet on spindle knot after collection.	84
Figure 4-23. Water spray on connected spindle knots.	86
Figure 4-24. Water droplets on spindle knot fiber.	86

Figure 4-25. Dodecane drops on groove fiber	88
Figure 4-26. Water drops on grooved fiber	88
Figure 4-27. Dodecane spray on grooved fiber	89
Figure 4-28. Water spray on grooved fiber.....	89
Figure 4-29. SEM image of the spandex used in the experiments described in the text.	91
Figure 4-30. Mering of static water droplets on spandex yarn over time.	92
Figure 4-31. Microflow mode created for droplets on multifilament yarns.	94
Figure 4-32. The time required for two drops to coalesce is shown versus the integrated term IL , the numerical intergral multiply the distance between the two droplets.	95
Figure 4-33. The web of a Basillica spider from Lake Raleigh, Raleigh, NC is shown along with the support structure and the net portion of the web.....	97
Figure 4-34. The coalescence of water droplet from mist on the support structure yarns from the web of a Basillica spider.	98
Figure 4-35. The designed fiber structure.....	100
Figure 4-36. Possible yarn morphologies that could be used for this project.....	100
Figure 4-37. The possible fabric structures.....	101

1. INTRODUCTION

Liquid aerosols are receiving more and more attention since they are a major component in air pollution and terrorist attacks due to the threats involving aerosol. These can have severe influence on the public psychological and physiological health. To protect those people who are exposed to life threatening liquid aerosols, intensive studies need to be conducted to understand the principle of wetting of liquid aerosols and to design and produce aerosol barriers in order to collect and eliminate liquid aerosols.

Spider webs can collect liquid aerosols, which can be observed in early morning. Numerous aerosol droplets collected on spider silks form larger droplets, which can be easily removed by slight vibration offered by breezes or transferred to a highly absorbent fabric. This phenomena brings new hope for people living in dry areas who need new water resources other than rain and underground water, and for those who are living in highly air polluted areas, which require highly efficient filters installed in all types of discharge systems in order to purify waste gas generated by modern civilization.

Spindle knots have received intensive interest recently after they were found to exist on wetted *cribellate* spider silk¹. Since then, there have been two dominant directions of research of the spindle knot silk web. One group of researchers is trying to mimic the spider web morphology through chemical engineering to create the spindle knot shapes with a certain degree of roughness on fibers,¹⁻⁴ which widened people's mind about the amazing natural world and indicated the hope of mimicking nature for industrial production. For example, utilization of the properties of spindle knot fibers to collect water⁴ or to collect oil from water-oil mixtures have been reported recently⁵. Another direction is trying to

understand the water collection principle through computational modeling based on Gibbs free energy in order to utilize the science in applications such as water/oil separation, filtration, superhydrophobicity, liquid collection and micro-fluid delivery.⁶ This research is attempting to understand the fundamentals for nature and created a better design for commercial applications and to scale up these findings.

In the 1970s, Carroll studied the shape of symmetric barrel shape droplets on cylinder fiber with details including contact angle, volume, and Laplace pressure using the Laplace equation and the geometric profile; exact solutions can be directly used to describe of the shape of a droplet on the cylindrical part of the spider web in today's study as well as providing one method for calculating the profile of symmetric droplets on conical shaped fibers⁷. The shape of symmetric droplets on an ever expanding cone with no end has been studied by Michielsen et al. based on Carroll's work⁶. The volume of the droplet and the Gibbs free energy of the droplet on conical fiber system were derived, which can estimate the location of the symmetric small droplets on conical fibers.

In nature, almost all spider webs can collect moisture from air but not all spider webs have spindle knots on them. Also, according to Michielsen et al.'s findings, the directional motion of droplets is not always towards to the widest end of the cone. Therefore, it is very important to understand the basic science about spider silks and liquid aerosols. This project will achieve the following objectives:

- (1) Understand the mechanism of moisture collection on spider webs.
- (2) Design and optimize the structure of aerosol liquid barriers and produce super-aerosol-phobic textiles.

2. LITERATURE REVIEW

In nature, spider webs exist widely and have been shown to have high strength and elasticity⁸. Many studies have worked on mimicking spider webs in order to get the desired strength and elasticity⁹⁻¹³. Recently, the morning dew collection on spider webs has attracted many researchers in the pursuit of the production of spindle knots using chemical and Rayleigh instability properties.^{4-6,14} In order to understand the mechanism of moisture collection on spindle knots, the fundamental and recent progress in liquid interface, solid interface, the interactions between liquid and solid, and droplets related with this research need to be reviewed to understand the basic science of wetting. At the same time, the droplet wetting behavior on cylindrical and conical fibers is reviewed. In addition, recent updates in engineering spider silk are reviewed at the end of this section. As the most important factor, the liquid interface will be introduced first.

2.1. Liquid Interface

2.1.1. Surface Tension of a Liquid

Surface tension is chosen as the first parameter to be discussed because it is the most important factor in determining the interaction between a liquid and a solid. The surface tension of a liquid is caused by the unbalanced intermolecular forces applied on the surface molecules, which are pulled to join the liquid but not the other medium, as shown in Figure 2-1. To keep those surface molecules in balance, surface tension is generated by the networked intermolecular forces among molecules. For the outermost layer of liquid molecules, their unbalance depends upon the properties of both media, of which the surface is the common boundary. Therefore, surface tension is the joint property of two media.¹⁵

Generally, the surface tension of a particular liquid refers to the surface tension of the liquid in contact with its own pure vapor at the same temperature. The direction of surface tension is parallel to the surface, which can be explained from a thermodynamic point of view and a mechanical point of view.¹⁶ From the aspects of thermodynamics, surface tension is the excess free energy due to the presence of an interface between bulk phases. For the molecules at the boundary of vapor and liquid, as shown in Figure 2-1, part of the bonds are missing compared with the molecules inside bulk liquid, which leads to an increase of free energy. Therefore, surface tension can be written as

$$\gamma_{LV} = \left(\frac{\partial G}{\partial A} \right)_{T,V,n} \quad 2.1$$

where V is volume of the system, n is number of molecules, T is temperature, A is the surface area. Therefore, γ_{LV} is the energy needed to increase the interfacial area by one unit. Its unit is mass per time squared and it is usually expressed in force per unit length (N/m) or energy per unit area (J/m^2). From the mechanical aspect, a force tangent to the surface is needed in order to create a new surface. The direction of the surface tension can also be explained using the virtual work principle. To keep the shape of the surface, the surface tension tends to generate work to resist any outside interference by changing the surface area. Therefore, the direction of the surface tension has to be parallel to the surface of the liquid.

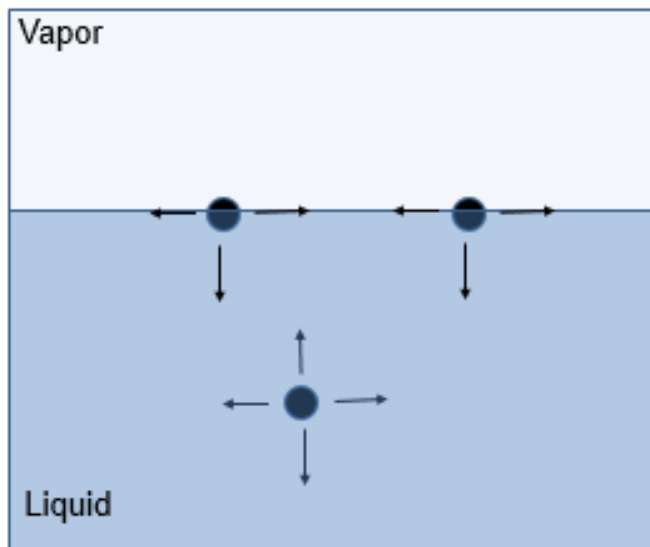


Figure 2-1. The scheme of surface tension.

From the definition of surface tension, it is obvious that the surface tension depends on the intermolecular forces, which is determined by the molecular properties and the environmental factors such as temperature and pressure. Surface tension of pure liquids and mixtures can be measured by several methods.

In the 1920s, surface tensions of liquids were measured using capillary tubes, virtual capillary tubes, vertical plates, a plate and cylinder, small pendant drops, large pendant drops, sessile drops and bubbles, Jaeger's method, drop weight, pull of vertical film, pull on vertical plate, pull on ring, adhesion plate, pull on sphere, oscillating drops and bubbles, vibrating jets, and ripples.¹⁵ Nowadays, most of the methods are commercially available from many instrument companies and use computers and software to simplify analysis. Theoretically, the value of surface tension of a liquid can be obtained through Hildebrand parameter¹⁷, expressed as

$$\gamma_{LV} = \delta^2 V^{1/3} / C \quad 2.2$$

where C is a constant that depends on the type of molecule. V is molar volume. δ is

Hildebrand parameter or solubility parameter. Equation $\gamma_{LV} = \delta^2 V^{1/3} / C$

2.2 is only valid for nonpolar non-associated liquids. This can be improved by using partial cohesion parameters that treat Van der Waals, dipole-dipole and hydrogen bonding interaction separately.

Surface tension plays the dominant role in keeping the liquid surface profile, which creates a pressure difference between the liquid and its vapor across the interface. The pressure difference is called the Laplace pressure.

2.1.2. Laplace Pressure

Under the assumption that the surface interface is in equilibrium, the Laplace pressure has been introduced by Young and Laplace¹⁸ as the pressure between the inside of the droplet and the outside of the curved surface, which is caused by the surface tension. Based on the principle that the work done by surface tension equals the work done by Laplace pressure due to conservation of energy, the Laplace pressure equation can be derived by taking a small section of an arbitrarily curved surface, as shown in Figure 2-2. The two principal radii of curvature are marked by R_1 and R_2 , which are assumed to be constant when the section of surface is small enough. When the surface is displaced a small distance outward, the change in area can be expressed as

$$\Delta A = (x + d_x)(y + d_y) - xy = xd_y + yd_x \quad 2.3$$

The work done by surface tension in forming this additional amount of surface is

$$W = \gamma(xd_y + yd_x). \quad 2.4$$

The pressure difference ΔP across the surface can balance the work by surface tension, which is

$$W = \Delta P x y d_z . \quad 2.5$$

Next the geometrical relationship in similar triangles,

$$d_x = \frac{x d_z}{R_1} \quad 2.6$$

and

$$d_y = \frac{y d_z}{R_2} \quad 2.7$$

are plugged into equation $W = \gamma(x d_y + y d_x)$.

$$2.4 \text{ and } W = \Delta P x y d_z .$$

2.5 to give

$$\Delta P = \gamma \left(\frac{1}{R_1} + \frac{1}{R_2} \right). \quad 2.8$$

From equation 2.8, one obtains

$$\Delta P = \frac{2\gamma}{R} \quad 2.9$$

for a liquid-vapor interface when R_1 and R_2 are equal, such as for the spherical surface of droplet. At the same time, for interface that has infinite R_1 and R_2 , i.e. for a planar surface, the Laplace pressure is zero across the surface interface.

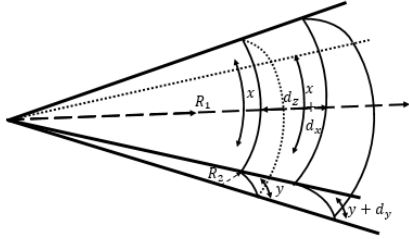


Figure 2-2. The condition for mechanical equilibrium for an arbitrarily curved surface. ¹⁸

Unlike surface tension, the Laplace pressure is determined by the shape of the liquid interface. However, neither of these factors is constant for a change of environmental factors, such as temperature and pressure, which can be explained in the thermodynamics of liquid interface.

2.1.3. Thermodynamics of Liquid Interface

For a one-component system, as mentioned in the definition of surface tension, the surface free energy per unit area G^S can be used to obtain entropy at constant pressure and temperature as

$$dq = TdS = TS^S dA \tag{2.10}$$

where S^S is the surface entropy per unit area of the surface. At constant pressure,

$$\left(\frac{\partial G}{\partial T}\right)_P = -S \tag{2.11}$$

therefore

$$\left(\frac{\partial G^S}{\partial T}\right) = -S^S. \tag{2.12}$$

The total surface enthalpy per unit area H^S is

$$H^S = G^S + TS^S \tag{2.13}$$

The approximation

$$H^s = E^s \quad 2.14$$

can be made to get total surface energy

$$E^s = G^s + TS^s = \gamma - T \frac{d\gamma}{dT}. \quad 2.15$$

It is apparent that the total surface energy E^s is larger than the surface free energy since the surface tension of most liquids decreases with increasing temperature. The most well-known relationship was developed by Eötvös:

$$\gamma V^{2/3} = \kappa(T_c - T) \quad 2.16$$

where V is the molar volume, κ is a constant that is close to 2.1 ergs/K for most liquids, T_c is the critical temperature, at which liquid and vapor have same density.

When temperature increases, the molar volume will decrease because of the decrease of the material density due to thermal expansion. All these factors lead to the decrease of surface tension. Another relationship originated by van der Waals in 1894 and developed further by Guggenheim is

$$\gamma = \gamma^\circ \left(1 - \frac{T}{T_c}\right)^n \quad 2.17$$

where n is 11/9 for many organic liquids and γ° is surface tension of the material at temperature T_c .

For the interface between a liquid's surface and its own vapor, molecules are constantly evaporating and condensing as molecules hit the surface and escape or are captured.¹⁸ In order to study the wetting behavior of liquid droplets, maintaining the balance of evaporation and condensing is very important. Based on the free motion of liquid molecules on liquid

surface, it is worthwhile to look into the alignment of molecules, especially for those molecules that have large differences between two sides of the molecule, and may have a large effect on the surface chemistry and surface interactions.

2.1.4. Orientation at the Interface

For a liquid interface, orientation of molecules should be taken into consideration in the study of liquid interface. Hardy and Harkins introduced the “force” concept and Langmuir developed the concept quantitatively¹⁸, with the principle of independent surface action, which has been used by many researchers over the years. Ethanol was taken as one example in Adamson’s book, shown as Figure 2-3. In the first case (a), the surface presented would comprise hydroxyl groups whose surface tension should be about 0.19 N/m. In case (b), a surface energy that of a hydrocarbon should be about 0.05 N/m. There is a difference of 0.14 N/m, or about 3×10^{-20} J per molecule. Therefore, the orientation of the ethanol molecule at the droplet-vapor interface prefers case (b) based on the lowest Gibbs free energy. The experimental value of the surface tension of ethanol is 0.022 N/m, which is closer to the surface tension of a hydrocarbon.

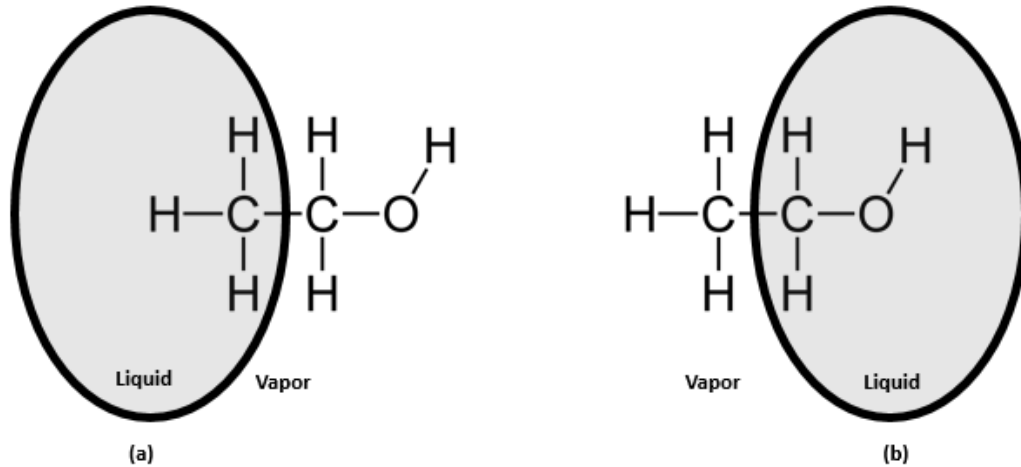


Figure 2-3. Two possible chemical orientations at ethanol liquid interface.

2.2. Solid Interface

Wetting of fibers is not only related to the liquid surface but also related to the solid surface.

In this chapter, the concepts and techniques related to solid surface will be introduced.

Similar to the liquid interface, the surface energy is the first concept to be introduced.

2.2.1. Surface Energy of Solids

For the surface tension of the liquid, it is convenient to take it as surface energy. However, in solid interface, it is desirable to consider an independent, more mechanical definition of surface stress. In Adamson's book, it is defined by one case as "If a surface is cut by a plane normal to it, then, in order that the atoms on either side of the cut remain in equilibrium, it will be necessary to apply some external force to them. The total such force per unit length is the surface stress."¹⁸ The surface stress is denoted as

$$\tau = \frac{d(AG^S)}{dA} = G^S + \frac{AdG^S}{dA} \quad 2.18$$

for an isotropic solid. For liquids at equilibrium, the relationship $\frac{dG^S}{dA} = 0$ is found and the

expression is same as equation $\gamma_{LV} = \left(\frac{\partial G}{\partial A}\right)_{T,V,n}$ 2.1.

2.2.2. Theoretical Estimates of Surface Energies

The calculation of surface energy varies with the type of the solid considered. In Adamson's book, the theoretical estimates of surface energies have been summarized by covalently bonded crystals, rare-gas crystals, ionic crystals, molecular crystals and metals. However, in the studies below, most solid surfaces are composed of polymers, such as nylon. Therefore, models for calculating the surface energy of the polymeric surfaces are needed.

Partial surface energy is very important to calculate the surface tension of polymeric surface, which assumes that surface tension of the surfaces is composed of different interactions including disperse, dipole-dipole and hydrogen bonding, which can be expressed as ¹⁷

$$\gamma = \gamma_d + \gamma_p + \gamma_h \quad 2.19$$

where $\gamma_d, \gamma_p, \gamma_h$ is the surface tension due to disperse forces, dipole-dipole interactions, and hydrogen bonds. These parameters can be calculated based on the relationship between surface tension and solubility parameters.

2.2.3. Surface Characterization Techniques

Unlike in liquids, the molecules on the surface of solids cannot move freely. The properties of a solid surface are not only determined by the chemical properties of the surface but also depend on the morphology of the surface, such as roughness, especially in wetting.

Generally, there are two major ways to characterize the surface of solids. Microscopy methods including scanning probe microscopies, field emission and field ion microscopies and low energy electron diffraction are widely used.¹⁸ Optical microscopy has a minimum spatial resolution of 250 nm, namely half the wavelength of visible light. Confocal microscopy can scan three-dimensional images from solutions, biological membrane and polymeric systems. Photo tunneling microscopy (PTM) can reach as high as 1 nm resolution vertically and one quarter of the wavelength of light in the lateral directions using the properties of evanescent waves created when light tunnels from a medium of higher index of refraction into one of lower index. Transmission electron microscopy (TEM) and scanning electron microscopy (SEM) have been widely used. TEM can resolve down to 1 nm and can characterize the structure by passing through a thin sample using electron diffraction. Compared with TEM, SEM can resolve down to 50 nm but it has a wide range in contrast and great depth of focus. Usually, SEM is the best choice to characterize when the sample surface is very rough.

2.2.4. Surface Modifications

To improve the physical and chemical properties of solid surfaces, there are numerous ways to modify the surface of the solids. In this study, the solids that are studied are polymeric fibers. Therefore, modification of fibers is the primary objective in this project, which includes coating, plasma treatment, and surface grafting. Coatings can improve the fiber surface properties but they often come off when there is any bending, heat change, abrasion, or other forces applied to it.¹⁹⁻²¹ Plasma treatment is very high cost in industrial production though it can be used to etch the fiber surface and produce active chemical groups for further

reaction.^{22,23} Chemical grafting on surfaces has been applied to several applications and proved to be cost effective²⁴⁻²⁶. Some modifications use a single step using chemicals that can react with the active groups on fiber surfaces, such as carboxyl groups and hydroxyl groups^{25,27-29}. The advantage of this approach is high efficiency and low cost. However, the active groups in many fibers are very limited. To cover the surfaces of fibers as much as possible, it would be better to have some initial modification on fibers to increase the number of the active groups. Some studies have used plasma to create initiators for chain growth polymerization²³. Other studies remove the hydrogen groups on fiber surfaces using chemicals for further polymerization, such as atom transfer radical polymerization (ATRP)³⁰. At the same time, some studies used polymers with many active groups to increase the reactivity of the fiber surface.^{24,31} Most methods used solvents, hazardous chemicals and multiple step reactions. None of these aspects satisfy the requirement of industrial production, which supposedly is the goal of all techniques introduced above. Therefore, chemical modification of the surface with low impact to the environment, longer stability and lower cost is the trend of surface modification.

2.3. Solid-Liquid Interaction

2.3.1. Introduction

After understanding the basic properties of the liquid interface and solid interface, the interactions between them are reviewed. There are many types of interactions, such as absorption and adsorption. However, contact angle and capillarity are the main focus of this

review. The Rayleigh instability is explained as a unique interaction between liquid and cylindrical solids at the end of this section.

2.3.2. Contact angle

The contact angle was originally described by Young, as given in equation 2.20³², which deals with the most common situation observed. A droplet was deposited a smooth surface, where the effect of gravity was ignored, as shown in Figure 2-4. It can be expressed as

$$\cos\theta_e = \frac{\gamma_{SV} - \gamma_{SL}}{\gamma_{LV}} \quad 2.20$$

where γ_{SV} , γ_{SL} , γ_{LV} are the interfacial surface tension between solid-vapor, solid-liquid, and liquid-vapor phases, respectively.

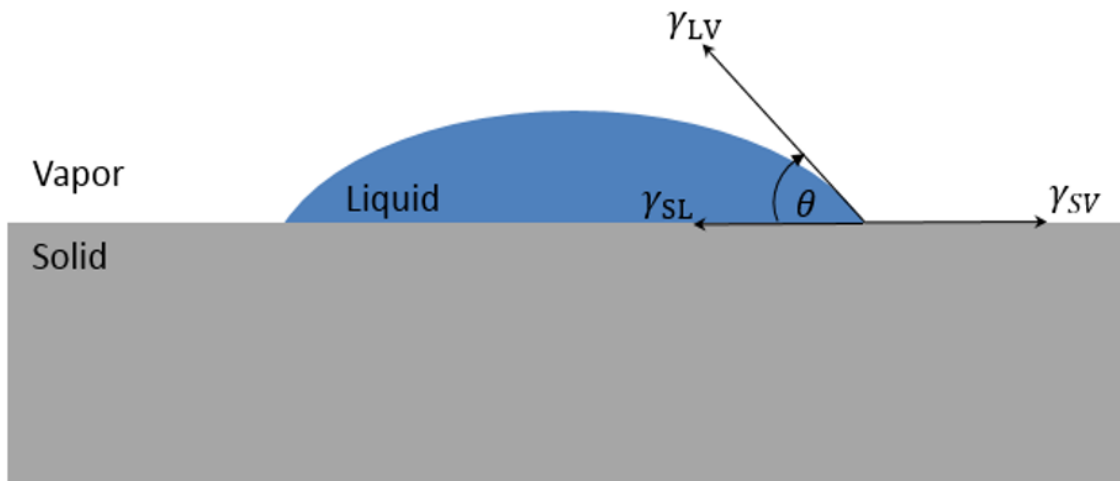


Figure 2-4. The scheme of contact angle.

Young's equation is based on equilibrium state of droplets on surface, namely

$$\lim_{\Delta A \rightarrow 0} \frac{\Delta G^S}{\Delta A} = 0 \quad 2.21$$

where ΔG^S is the change of surface free energy, ΔA is the change of area of the solid that is covered by the droplet. Therefore, the contact angle obtained from this approach is the contact angle of the equilibrium state. A limitation of Young's equation is that it only deals with smooth flat surfaces, which generally do not occur for most wetting situations, especially for this project, which deals with extremely small droplets on surfaces that are intentionally made to be rough.

The concept and modeling of contact angles on rough surfaces have been developed by Wenzel³³ and Cassie and Baxter³⁴, and are shown in Figure 2-5. The contact angle formed on a rough surface is referred to as the apparent contact angle, which is a milestone for the understanding of wetting behavior, especially in the field of textiles which are composed of many tiny pores created by fibers and yarns. In Wenzel's model, the apparent contact angle θ_r^w can be expressed as

$$\cos \theta_r^w = r \cos \theta_e \quad 2.22$$

where r is the roughness of the surface, the ratio of the total true wetted area of a rough surface to the area beneath the drop obtained by projecting the drop onto a plane.

In the Cassie-Baxter model, the apparent contact angle θ_r^{CB} can be expressed as

$$\cos \theta_r^{CB} = f_1 \cos \theta_e - f_2 \quad 2.23$$

where f_1 is the ratio of area in contact with the liquid over to projected area of the droplet.

f_2 is the area in contact with vapor divided by the projected area.

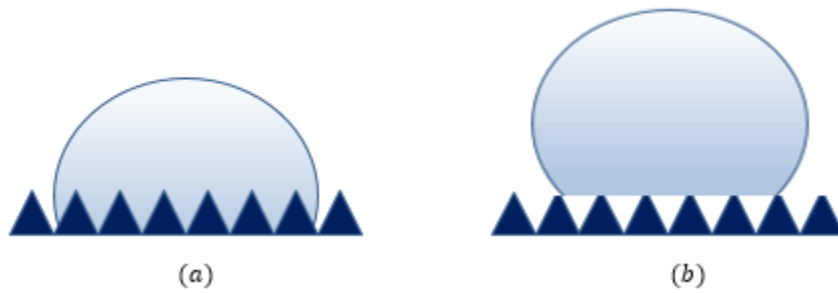


Figure 2-5. Liquid droplet on a rough surface: (a) Wenzel model, and (b) Cassie-Baxter model.

There have been some arguments on whether both models are valid^{35,36} due to differences between experimental results and those calculated based on Wenzel and Cassie-Baxter models. However, these arguments against both models are lacking in consistency in experimental conditions with the models built by Wenzel and Cassie-Baxter based on details in their experiments. Meanwhile, proving a model through experiment always requires extra care for lab conditions, parameter set up, and data collection.

Wenzel and Cassie-Baxter models have been regarded as milestones in liquid and solid interface area, which indicates that both surface chemistry and surface morphology can affect the wetting of the surfaces. Superhydrophobic surfaces can be obtained through increasing the surface roughness or decreasing the surface energy of the surface through approaches discussed in surface modification of solid interface. With known contact area between liquid and solid and between liquid and vapor, one can estimate the apparent contact angle on a surface, which offers chances to lower the cost in fabric design. However, there are limitations in Wenzel and Cassie-Baxter models. It is impossible to obtain the contact area in

roughness calculation without knowing whether there is complete wetting or incomplete wetting.

In this study, we assume all surfaces are smooth. The contact angle we used for simulation is based on experimental results obtained from lab. Therefore, there is no need to characterize the surface tension of each surface used in this research.

2.3.3. Capillarity

In wetting, the contact angle is not the only important parameter. In most cases, capillarity plays very important role in wetting. Capillary rise exists widely and is due to the surface tension as shown in Figure 2-6. For simplicity, it is assumed that small circular capillaries have a hemispherical meniscus. Which means the two radii of curvature are equal to each other and to the radius of the capillary.

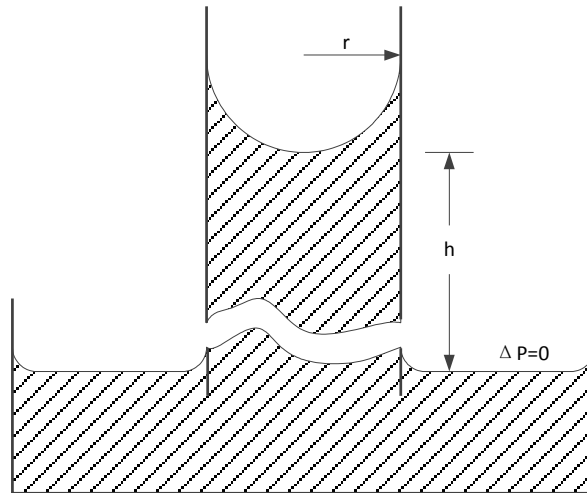


Figure 2-6. Capillary rise (capillary much magnified in relation to dish)¹⁸

In Figure 2-6, the Laplace pressure of the droplet is balanced by the hydrostatic pressure in a column of liquid in the capillary. Therefore,

$$\Delta\rho gh = \frac{2\gamma}{r} \quad 2.24$$

where $\Delta\rho$ is the density difference between liquid and air.

The capillary constant or capillary length is defined as

$$a^2 = \frac{2\gamma}{\Delta\rho gh} = r \quad 2.25$$

where h is the height of liquid column.

When the liquid contacts the capillary wall with angle θ , then the equation can be rewritten as

$$\Delta\rho gh = \frac{2\gamma\cos\theta}{r} \quad 2.26$$

Capillary length is very easy to obtain through image analysis, therefore, it is one of the most convenient methods to measure the surface tension of an unknown liquid. In textiles, capillarity plays very important role in wetting, which needs to be taken into consideration in each procedure in the finishing industry and in final applications.

Capillarity is also one of the most basic ways to determine textile wetting, which is generally called wicking³⁷⁻⁴³. The capillary flow driven by pressure P was first studied by Washburn⁴⁴, who studied the penetration of liquids into cylindrical capillaries. In this study, the relationship among the radius of capillaries r , P , and time t , length of the capillaries L , viscosity of the liquid μ and the coefficient of the slip ϵ is expressed as

$$\frac{dl}{dt} = P(r^2 + 4\epsilon r)/8\mu L. \quad 2.27$$

Washburn's study only focused on the moment after capillarity flow formed. Many other later studies examined the wicking of liquids into textiles from the first moment when a

droplet contacted with the yarns^{39,42,43,45-47} from experimental and theoretical points of view. In addition, wicking by yarn occurs at many open irregular channels. Pressure driven flow in open channels without walls have been studied⁴⁸. The closed model for wicking by a yarn is close to the pressure driven flow through a horizontal circular pipe, which is called the Hagen-Poiseuille law⁴⁹, as shown in Figure 2-7 . The volumetric flow rate can be expressed as

$$Q = \frac{\pi R^4}{8\eta} \frac{-\Delta P}{L} \tag{2.28}$$

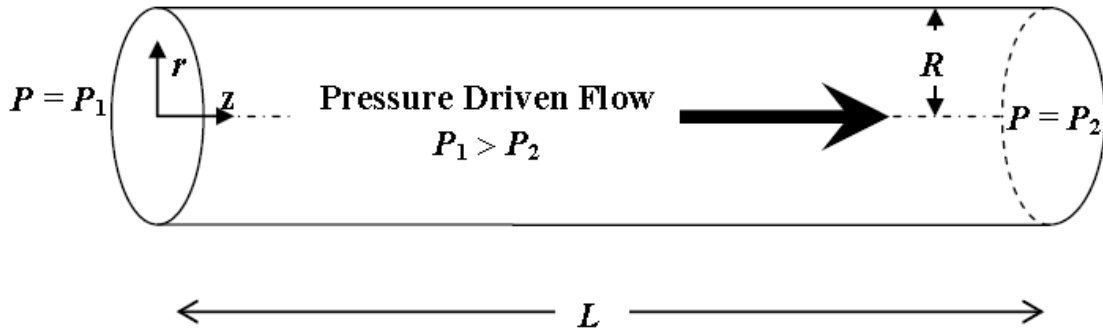


Figure 2-7. The pressure driven flow model used by Hagen Poiseulle Law.

where R and L is radius and length of the pipe, ΔP is the pressure difference between P_1 and P_2 . η is the fluid viscosity. Recently, flow rate analysis of a surface tension driven passive micro-pump has been conducted.⁵⁰ All the studies listed above indicate that the motion of the flow in a smaller space with a smaller velocity can be studied based on Hagen Poiseulle Law

just by multiplying with a shape factor. In this study, the fluid mechanical approach will be used to understand the wetting behavior of liquid on yarns, which is composed of numerous micro-channels.

When the yarn or fiber is saturated with liquids, special phenomenon called as Plateau-Rayleigh instability occurs, which can cause considerable trouble to wire coating industry but creates many opportunities for textile industry in producing engineered fibers.

2.3.4. Plateau-Rayleigh Instability

The Rayleigh instability was first studied by Lord Rayleigh in 1879¹⁸. It occurs in daily life, such as the water string from tap water. When a perfectly uniform coating is applied to the surface of a fiber, it breaks up spontaneously into small beads clinging to the fiber at regular intervals, which has a very important influence to wire coating industry⁵¹. The process is depicted in Figure 2-8. This process occurs because the liquid interface needs to minimize the total surface area. The quantitative study on the length of intervals, height of droplet and volume of the droplets have been studied thoroughly⁵¹⁻⁵³. This phenomena indicates one approach of modifying the morphology of the fiber.

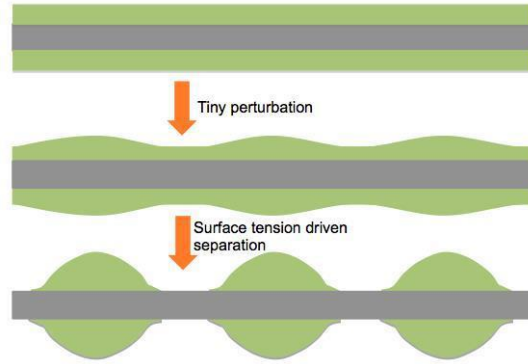


Figure 2-8. A uniform coating on a fiber experiences small fluctuations in its radius. To minimize free energy, this disturbance grows into nearly equally spaced drops.⁵²

2.4. Droplets

2.4.1. Introduction

In wetting behavior studies, the droplet is the most basic unit. In this part, the interaction between droplets, and the droplet on different curved surfaces including cylinder, cone, and spindle knots will be introduced.

2.4.2. Interaction between droplets

Droplets not only interact with solid surfaces, but also interact with each other and coalesce when the distance between two droplets is sufficiently close. Coalescence of two or more droplets has been studied using three techniques, including microchannels, electrowetting arrays, and wettability gradients.

Microchannels are widely used to study the behavior of droplets in coalescence phenomena.

The mechanism is to merge two droplets in an immiscible solvent by differences in their velocity. Figure 2-9 shows the scheme of the microfluidic channel used for the droplet coalescence process⁵⁴. DP_1 and DP_2 can be same or different liquid. CP is the solvent for DP_1

and DP₂. The delivery speeds for DP₁, DP₂ and CP are different. Two droplets can merge at certain distances after being delivered to the microchannel. In this figure, both straight channel and disperse channel were applied in order to control the velocities.

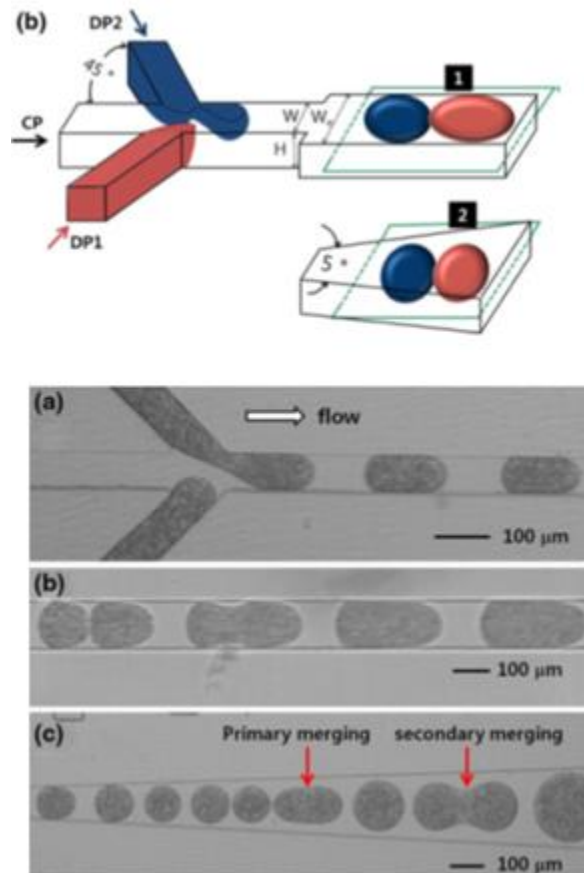


Figure 2-9. Microfluidic channels used for droplet merging process.⁵⁴

Electrowetting arrays are also used to control the merging of two droplets using static forces.

⁵⁵ Figure 2-10 shows side and top schematic views of the electrowetting mixing actuator.

Briefly, the actuator uses static forces between the droplet and the electrode to change the

profile of each droplet so they can merge. Figure 2-11 shows an easier way to actuate the merger of two droplets by using free electron charges in droplets. So for this approach, an electrolyte should be present in both droplets.

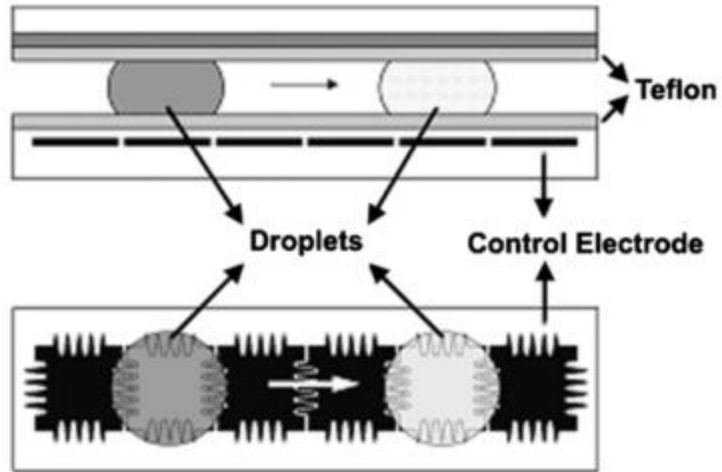


Figure 2-10. Side and top schematic views of electrowetting-based mixing actuator.

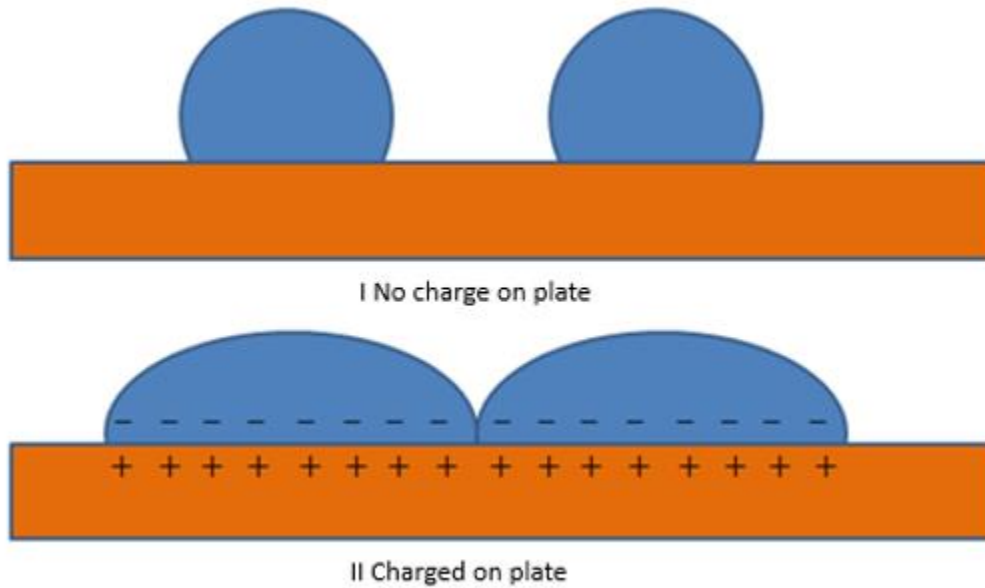


Figure 2-11. The scheme of mechanism of electrowetting array

Both microchannels and electrowetting arrays suffer from deficiencies. First of all, both of them are in closed systems, which means that merging of the surfaces is confined by limited space and even extra factors, such as the static force in electrowetting array. Secondly, both approaches are passive. If the objective is to observe the spontaneous merging, neither of them is suitable.

Unlike these two approaches, the wettability gradient approach⁵⁶ is an open system. Figure 2-12 shows the wettability change on the wettability gradient, which can be used to move the droplet (II) towards droplet (I) from certain distance d . The spontaneous motion of droplet II on wettability gradient is driven by Gibbs free energy. The preparation of a wettability gradient using vapor-diffusion technology was discussed by Lai et.al.⁵⁷ Compared with the

previous two approaches, this approach uses an open system, which enables us to understand spontaneous merging.

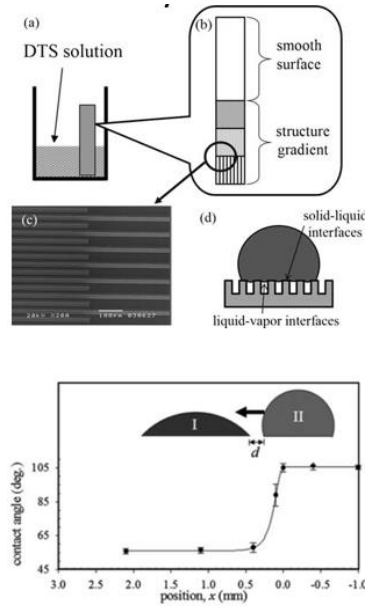


Figure 2-12. Static contact angles of the wettability gradient surface and initial positions of the moving droplet (I) and stationary droplet (II)⁵⁶.

All those studies focus on the coalescence of droplet in other medium or on a flat surface without consideration of droplet on curved surface or much smaller substrate, which is very often available on textile surfaces.

2.4.3. Precursor of droplets

In the coalescence of two droplets, the precursor film, if it exists, is a very important factor to take into account because it determines the critical distance for merging of two drops. The precursor film length is defined as the distance between contact line and the lip of the precursor, as shown in Figure 2-13⁵⁸. A constant thickness and a constant contact angle at contact line of the precursor have been widely assumed.⁵⁹

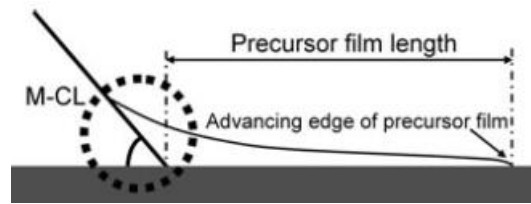


Figure 2-13. Precursor film of a spreading droplet (M-CL: motion of contact line)

The existence and length of precursor films have been studied by many authors.⁵⁸⁻⁶² The length of the precursor film is theoretically predicted and empirically expressed by Harvet & de Gennes and Kavehpour et al.⁵⁹ They indicated that the length of the precursor film is related to the capillary number.

The length of the precursor film has been detected using ellipsometry⁶³, which can detect as small as 0.1Å. For small non-volatile droplets (with a volume of around 10^{-4} μl) spreading on silicon wafers, the radial extent, ℓ_t , increases with time as \sqrt{Dt} . Where D is the diffusion

coefficient related to a molecular thickness of the precursor film. t is the time after placement of the droplet. The thickness of the precursor film in this case is of molecular thickness. This equation has been widely accepted by later work⁶⁴. In this study, the length was evaluated by the analysis of a time series of the brightness data by the observation of a fringe pattern with the elliptic of polarization interferometer. The velocity of the droplets U_{CL} was controlled by a temperature gradient. Thus, from Figure 2-14, the length is affected by temperature and capillary number Ca . $\partial T / \partial x$ in Figure 2-14 is the temperature change along the length of temperature gradient.

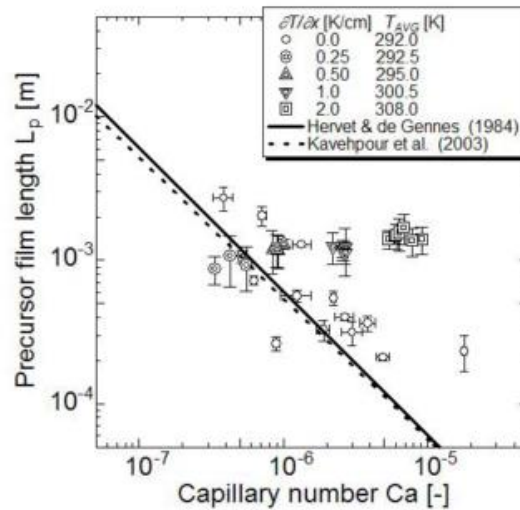


Figure 2-14. Precursor film length against the non-dimensional Capillary number.

Besides, the precursor of nano-droplets were described through molecular dynamic modeling by Webb et al.⁶⁵, as shown in Figure 2-15.

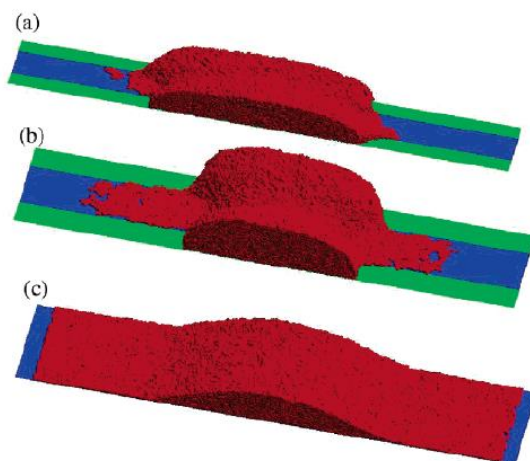


Figure 2-15. Image of simulation of polymer droplets on surfaces.

Though the above studies of precursor films were studied theoretically, none of them can demonstrate strong proof of or absence of a precursor film using experiments. It could be caused the difficulty of setting experiment such as liquid vapor equilibrium state. Also, it requires high-resolution characterization. The liquid precursor film has been clearly captured by Ju et al. using ionic liquid⁶⁶, as shown in

Figure 2-16. But the precursor here is not the precursor we discussed above because the precursor in this study is caused by the electrical force offered by the electrical field, which is shown in

Figure 2-16. Anyway, using ionic liquid to observe the wetting behavior of droplets is very inspiring.

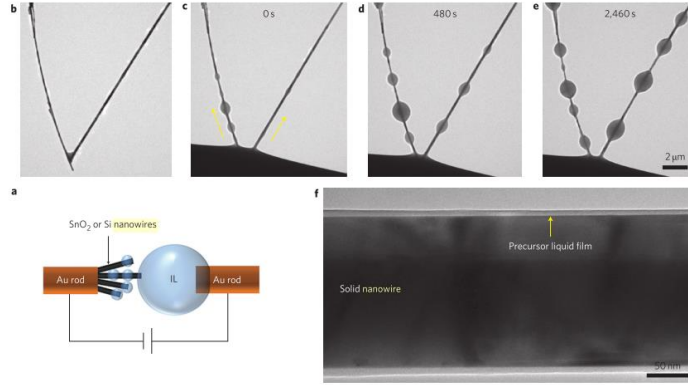


Figure 2-16. Ionic beads and liquid precursor film.

In this study, the critical distance for two droplets merging with each other will be a good answer to whether a precursor exists and if it is important to droplet wetting.

2.4.4. Droplet on a cylindrical fiber

The shape of a droplet on a cylindrical fiber has been studied^{7,67,68}. The first droplet profile was solved by Carroll. The shape is described in Figure 2-17. The volume of the droplet is expressed as

$$V = \frac{2\pi x_2}{3} \left(2a^2 x_1 + 3ax_1 x_2 + 2x_2^2 E(\phi, k) - a^2 x_1^2 F(\phi, k) + \frac{x}{x_2} (x_2^2 - x^2)^{0.5} (x^2 - x_1^2)^{0.5} \right) \quad 2.29$$

where

$$a = \frac{x_2 \cos \theta - x_1}{x_2 - x_1 \cos \theta} \quad 2.30$$

$$k^2 = (x_2^2 - a^2 x_1^2) / x_2^2 \quad 2.31$$

$$x^2 = x_2^2 (1 - k^2 \sin^2 \phi) \quad 2.32$$

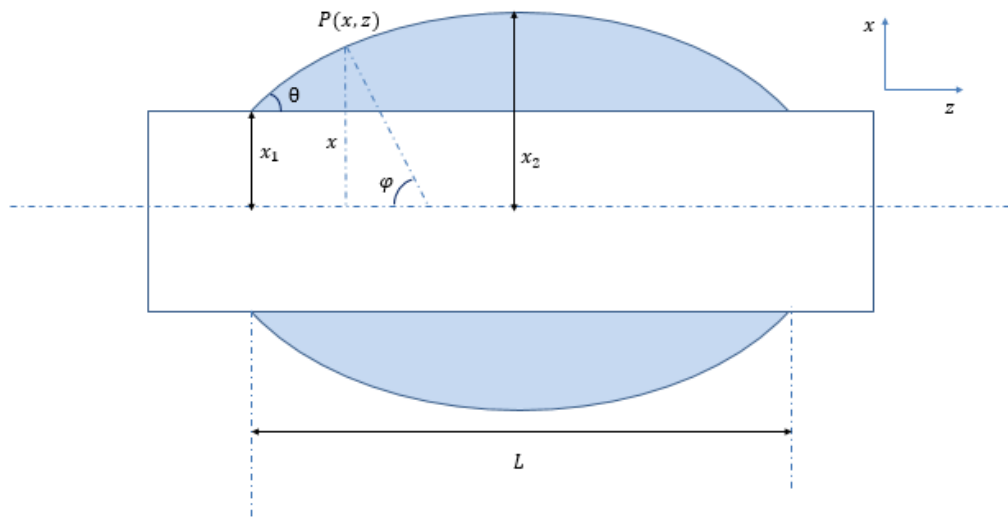


Figure 2-17. The droplet prolife on a cylindrical surface.

In this study, Carroll only took the barrel shape drop into consideration. Afterwards, he studied the transition conditions to clamshell shape drops through experiments and found this transition is caused by the relationship between the contact angle and fiber radius. Under the condition that the reduced volume (the volume of the droplet divided by the fiber radius) is large enough, the barrel shape is the preferred conformation. When the reduced volume decreases, a transition to a clamshell shape will occur. The critical value of reduced volume at which this stability transition occurs depends upon the equilibrium contact angle.⁶⁷

Recently, a public domain computer program, Surface Evolver⁶⁷ has been used to determine the stability of droplets through numerical approach, which calculates the area of barrel and

clamshell shapes using computer and minimizes the surface free energy to determine the final profile of the droplet. The procedure is shown in Figure 2-18.

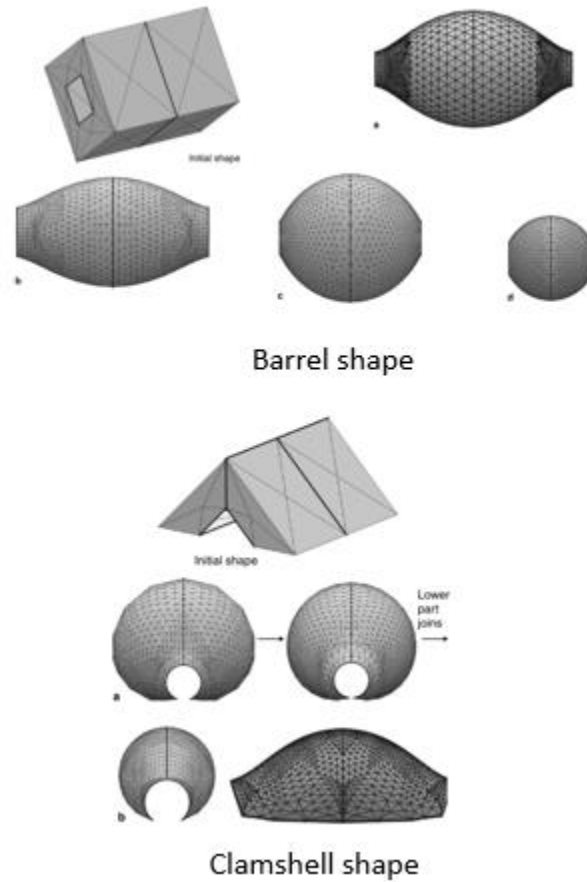


Figure 2-18. The procedure of Surface Evolver for barrel shape and clamshell droplet⁶⁷.

2.4.5. Droplets on conical fiber

Following Carroll's work, Michielsen et al.⁶ studied the prolife of barrel shaped drops on conical fibers, which revealed that these droplets can move spontaneously on a cone, as

shown in Figure 2-19. The barrel shape has two possible situations classified according to the half cone angle and contact angle of the droplets. When contact angle is bigger than half cone angle of the droplet, it belongs to left situation (a). When contact angle is smaller than half cone angle, it belongs to the right situation (b). The two situations simplify the integral of the droplets profile easily. Michielsen et al. recognized that a drop could not climb a cone indefinitely and conducted a more careful study on the directional motion of droplets on conical fibers⁶. This study indicated that a droplet on a conical fiber will move to a location where the Gibbs free energy is a minimum. This location depends on the cone half angle, Young's contact angle between the droplet and the cone, and the droplet volume. This research guided us to adjust the surface tension of the spindle knots and cone angle of the spindles in order to ensure the lowest Gibbs energy occurs at the widest point on the spindle knots. The expression of volume and Gibbs free energy are

$$V_i = \frac{\pi x^3}{3} n_n [(2a_i^2 + 3a_i n_n + 2n_n^2)E(\varphi_i, k_i) - a_i^2 F(\varphi_i, k_i) + \frac{(n_n^2 - 1)^{0.5} (1 - a_i^2)^{0.5}}{n_n}] \quad 2.33$$

$$G = \gamma_{LV} \{ 2\pi x_2 [(a_I x_1 + x_2)E(\varphi_I, k_I) + S(a_{II} x_3 + x_2)E(\varphi_{II}, k_{II})] - \frac{\pi}{\sin \alpha} (x_3^2 - x_1^2) \cos \theta \} \quad 2.34$$

For region I (the boundary condition is given by point A)

$$k_1 = \frac{2[x_1 \cos(\alpha + \theta)] - x_2}{x_1^2 - x_2^2} \quad 2.35$$

$$k_2 = \frac{[x_1 - x_2 \cos(\alpha + \theta)] x_1 x_2}{x_1^2 - x_2^2} \quad 2.36$$

$$a_I = \frac{x_2 \cos(\alpha + \theta) - x_1}{x_2 - x_1 \cos(\alpha + \theta)} \quad 2.37$$

For region II (the boundary condition is given by point C)

$$k_1 = \frac{2[x_3 \cos(\alpha - \theta) - x_2]}{x_3^2 - x_2^2} \quad 2.38$$

$$k_2 = \frac{[x_3 - x_2 \cos(\alpha - \theta)]x_3 x_2}{x_3^2 - x_2^2} \quad 2.39$$

$$a_{II} = \frac{x_2 \cos(\alpha - \theta) - x_3}{x_2 - x_3 \cos(\alpha - \theta)} \quad 2.40$$

Based on these two equations, the Gibbs free energy trend along the distance from the tip of the cone can be drawn with a known volume droplet. In this study, Michielsen et al. only studied water drops on cones. Many other liquids need to be used to strengthen their explanation.

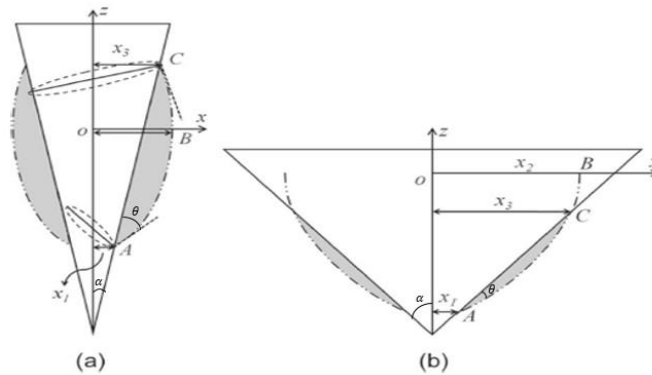


Figure 2-19. The schemes of the two possible cases in droplet wetting⁶.

Michielsen et al.'s study here only takes one situation in to consideration, which is when the droplet here sits symmetrically on the cone. However, unsymmetrical shape drops exist widely, which is called a clamshell drop in this study. The scenario of the clamshell droplet

sitting on cone has been reported, as shown in Figure 2-20. However, this study didn't give a good understanding of the shape of an oil droplet and the spontaneously motion of oil droplet⁵. At the same time, the R_1 and R_2 were marked incorrectly in the figure because they are the two radii's of clamshell shape.

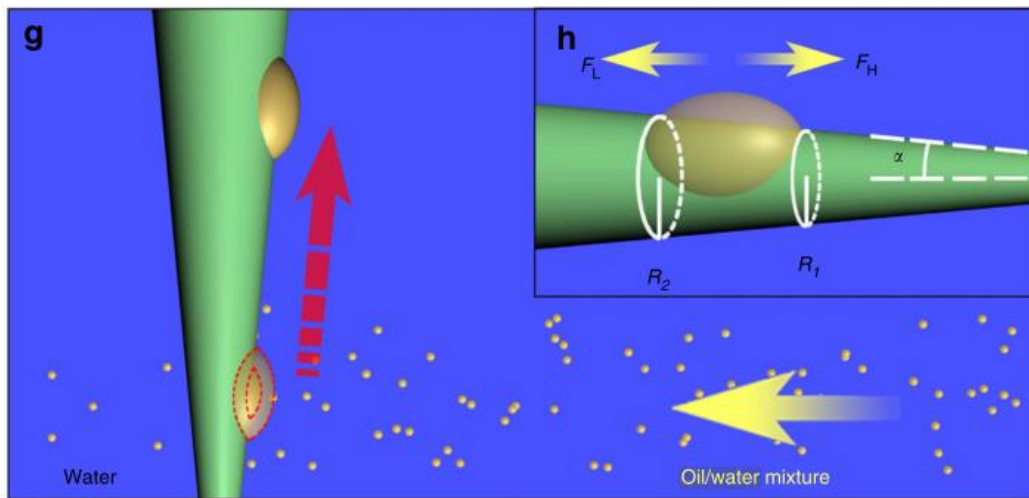


Figure 2-20. The spontaneously motion of clamshell droplet on cone⁵.

In this study, the clamshell droplet profile will be studied through experiment and theory study. At the same time, we will also study if the clamshell droplets will move to the widest part of the cone.

2.4.6. Droplets on spindle knots

Many studies have focused on reproducing spider silk through genetic engineering¹², protein regenerating⁹, and novel spinning¹³. However, these studies just focused on the elasticity

and tenacity of spider web in order to make super elastic and super strong fibers for applications such as body armor. Engineering spider webs from the aspect of moisture collection was initially reported by Jiang and his coworkers, who observed the yarns in the web of a *cribellate* spider, as shown in Figure 2-21. They found structures that they referred to as “spindle knots” and attributed the motion of water droplets on these yarns to the conical nature of the spindle knots. ¹

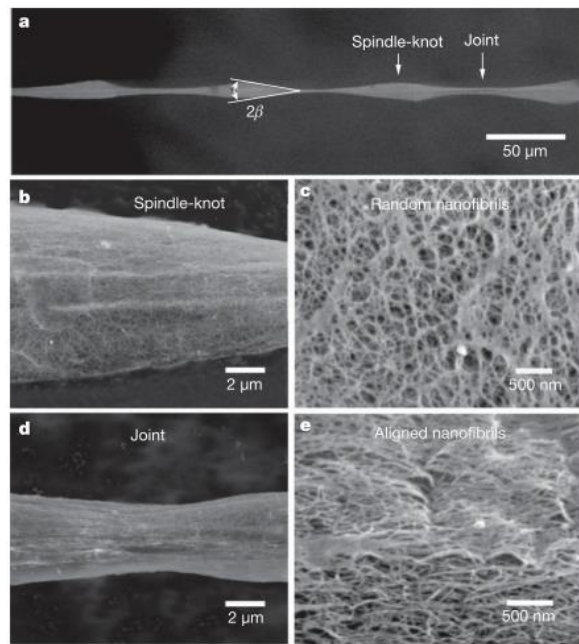


Figure 2-21. The structure of cribellate spider silk.⁴

They attempted to duplicate the spindle knot structure by dipping a fiber into a polymer solution, allowing the Rayleigh instability to produce polymer droplets, as shown in Figure

2-22, and then evaporating the solvent to leave behind a porous structure reminiscent of the spindle knots in the spider web. The procedure of making spindle knot shape was described in Figure 2-23.

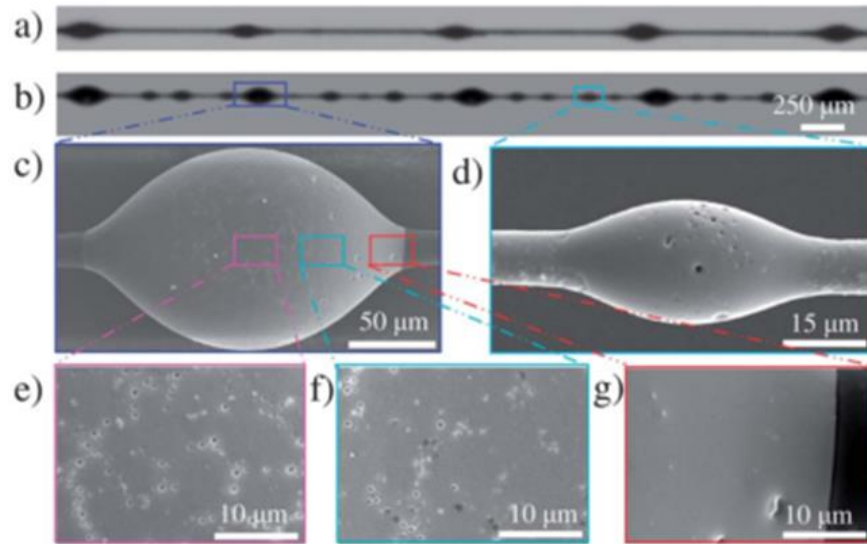


Figure 2-22. The profile of spindle knot built on fiber.

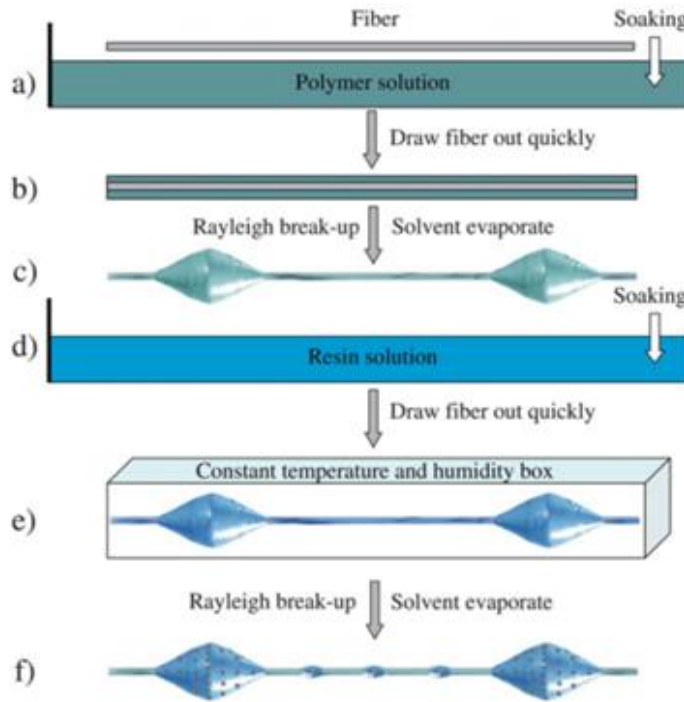


Figure 2-23. The procedure of making manmade spider silk with spindle knots.

In Figure 2-24, it took 1.8 s for the droplet to reach the edge of the spindle knot, but only 0.13 s for it to climb onto the spindle knot. Based on these results, they proposed that cylindrical sections of their fibers were much less effective at gathering droplets than the conical shaped spindle knots.

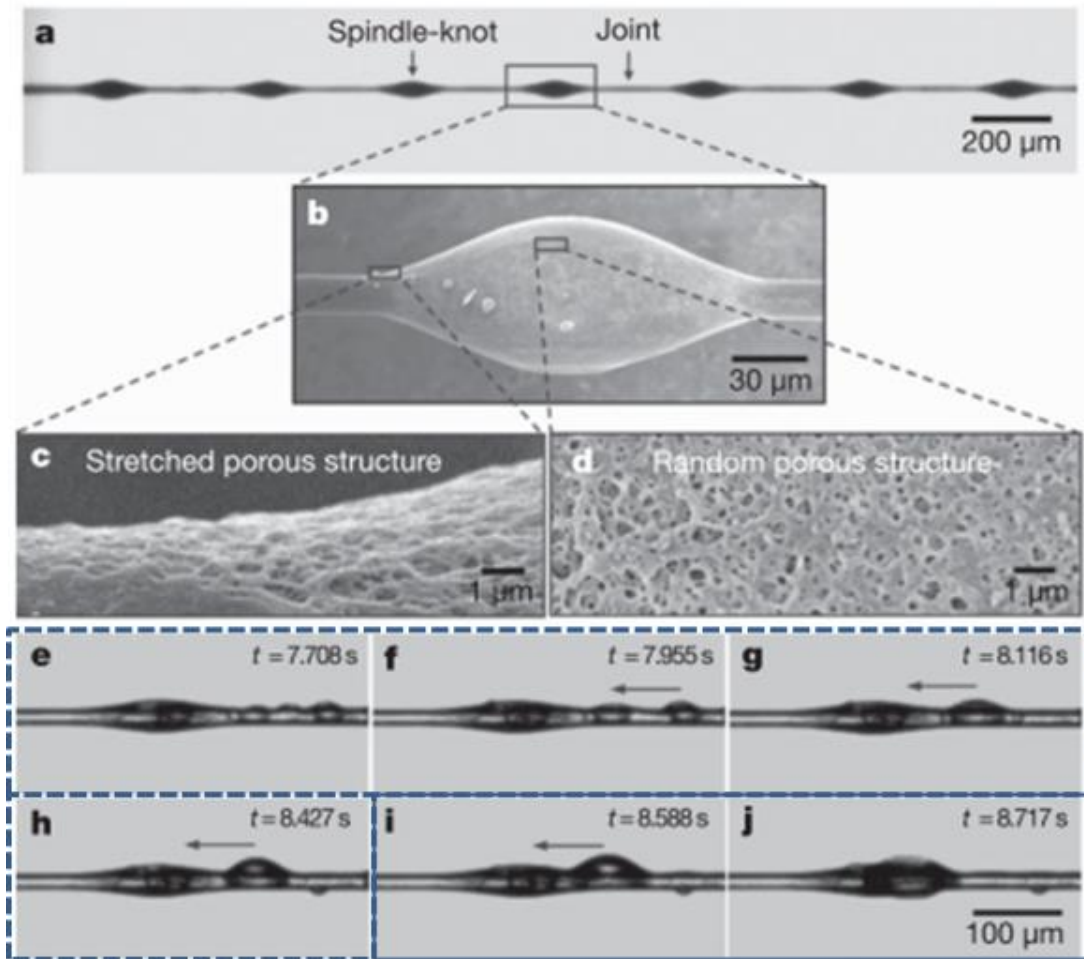


Figure 2-24. The structure of artificial spider silk and water collection. ⁴

This study was trying to mimick the spider web morphology through chemical engineering to create the spindle knot shape with a degree of roughness on the fibers, which pointed the way to new biomimicking applications for industrial production. However, in addition to the lack of efficiency during production, as mentioned above, considerable additional work is needed to further look at the basic science behind the moisture collection of spider silk from the four aspects discussed above. First of all, the author didn't give information about the droplet size.

The so-called mist has a diameter range from nanometer to millimeter, which is quite a different situation from the moisture collection of spider webs. To understand the wetting behavior of droplets on fibers, a more detailed droplet specification has to be given. Secondly, the principle of moisture collection of spider webs is not necessarily limited to spindle knots because the spider webs sample in this study is just one type out of thousands of types of spiders and their webs. However, most spiders' webs can collect moisture from air in early morning. Therefore, other mechanisms may be going on behind this phenomenon, which requires further study. Thirdly, the authors didn't explain the reason for the directional motion of water on spindle knots. Last but not least, the way of making spindle knots requires a lot of solvent, which prevents the practical application of this approach based on the consideration of environmental and economic cost.

2.5. Summary of literature review

From the literature reviewed above, the basic concepts of surface tension, Laplace pressure, and thermodynamics at the surface of liquid are explained, which laid the foundation for this project. At the same time, most classical models of wetting in the form of bulk droplets including capillarity and contact angles were explained and will be continually used in this project. Surface characterization techniques and approaches to improve the surface of solid were also reviewed, which provides information about how to modify the surfaces of fibers. At the same time, the cutting edge studies in wetting of spindle knots were also reviewed, which contribute many ideas toward the objectives of this study. However, there are many questions that have not been investigated, including

1. If every droplet regardless of volume, shape and surface tension will move to the widest part of the cone spontaneously?
2. If the spindle knots on the spider silk is the only reason that make spider webs collect droplets from mist?
3. If there is a critical distance between two droplets that make them merge with each other when they are not physically touching yet?
4. Is there a way to utilize properties of spider web and produce a manmade aerosol barrier?

3. EXPERIMENT

3.1. Materials

Deionized water, Kaydol (CBM group), glycerol (Sigma Aldrich) and dodecane (Sigma Aldrich) were used as liquid droplets. PMMA beads, MMA (purchased from Fisher Scientific) together with Irgacure 379® were used to make the spindle knots on fibers. Candle wax, (heptadecafluoro-1, 1, 2, 2-tetrahydrodecyl) trimethoxysilane (HFTT, Sigma Aldrich) and indium (RotoMetals) were used to create surfaces with different surface energies. Spandex yarn and nylon monofilaments were used as substrates for the droplets. The 0.5, 1 and 2 μ L microsyringes (Hamilton Company, Mircoliter 7002) were used to deposit droplets with specific volumes at microliter level on the surfaces. Microdrop® picoliter applicator (Microdrop®) was used to apply droplets at picoliter level to surfaces. B-100A high intensity UV lamp manufactured by UVP was used as the light source for polymerization. E-scope® USB camera purchased from Amazon and Phantom® High speed camera (Vision Research) were used to capture pictures of drops. A zoom lens (6.5X Zoom Lenses, 0.7 - 4.5X Magnification Range, Throlabs®) was used for the observation of picoliter droplet. A box light source was used as the light source for obtaining clear pictures. Newport® Motion stages (Model 423) were used to control the motion of the sample precisely.

3.2. Equipment

In this project, droplet deposition tools, contact measurement equipment, evaporation suppression chamber, microliter droplet observation system and picoliter observation system were built in our laboratory.

3.2.1. Droplet Deposition tools

Two deposition methods were used in this study, as shown in Figure 3-1, a perfume sprayer (Mist mode) and either a syringe or the picoliter applicator (droplet mode), depending on the droplet size needed. Both methods were used in several research stages. The mist mode more closely represents the practical situation but it is more difficult to control the parameters of the droplets. The droplet mode is easy to control droplet size, droplet deposition location and droplet frequency, but results in slow deposition.

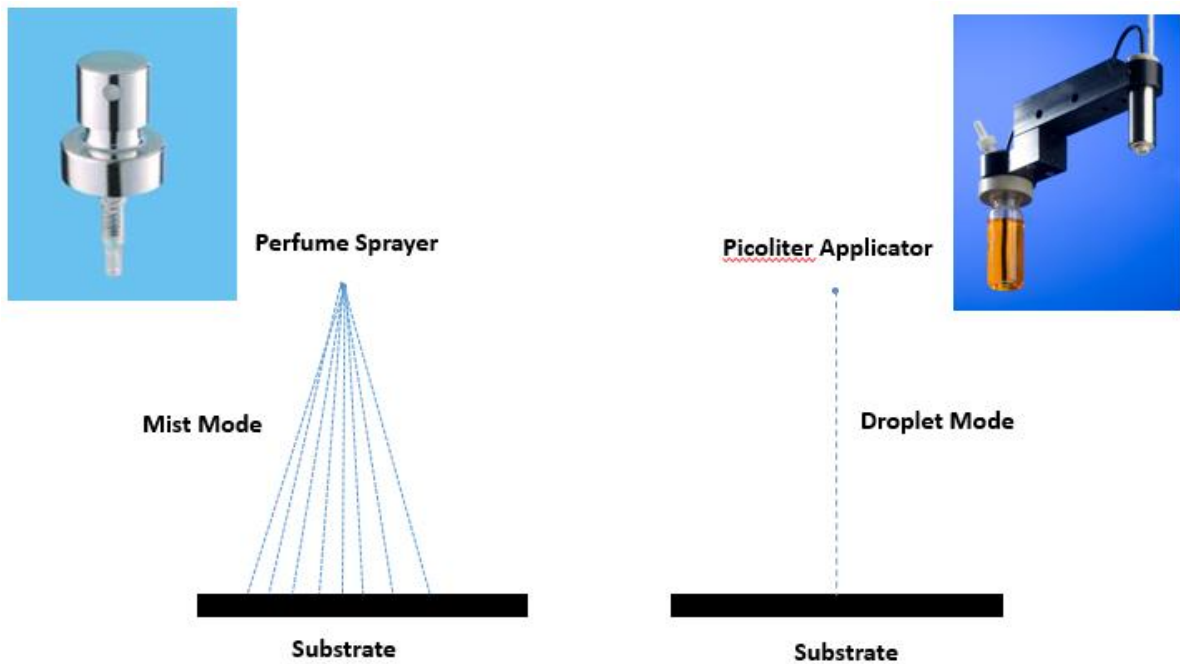


Figure 3-1. The mist mode generated by perfume sprayer and droplet mode produced by picoliter applicator are shown.

3.2.2. Contact Angle Measurement tools

The contact angle measurement apparatus was built in house using a USB microscope, Newport motion stage (Model 150), and other accessories, as shown in Figure 3-2. USB microscope is connected to a computer, which can deliver image of the drops to the computer. Newport® motion stage was used to control the position of the droplet precisely and to offer a black background for capturing clear pictures of liquid droplets. A sample holder was mounted on the motion stage in order to place sample. The contact angle of the droplet was measured as the angle between the flat surface and tangent line of the curvature at the contact line, as shown in Figure 3-3.

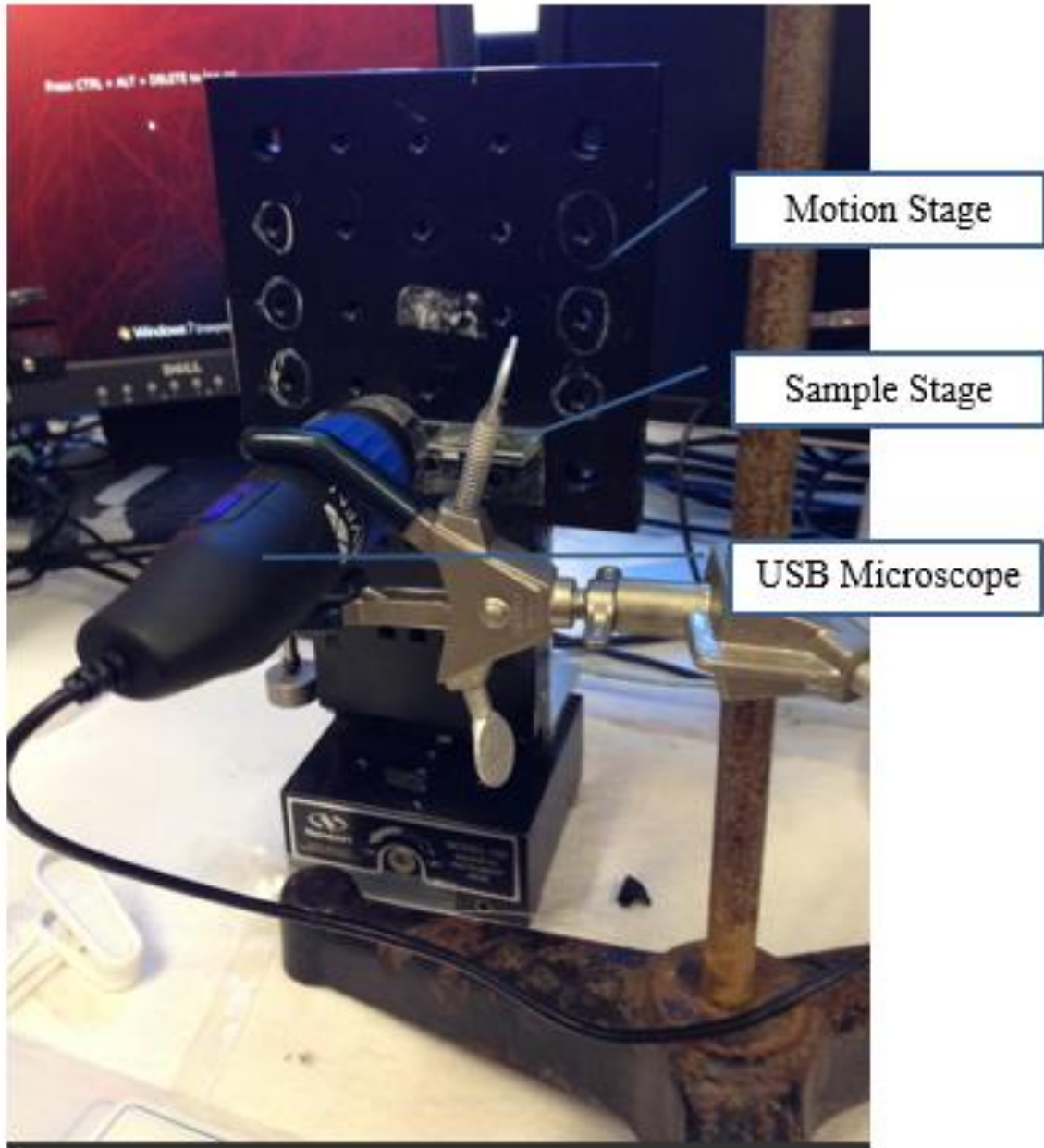


Figure 3-2. The contact angle measurement apparatus.

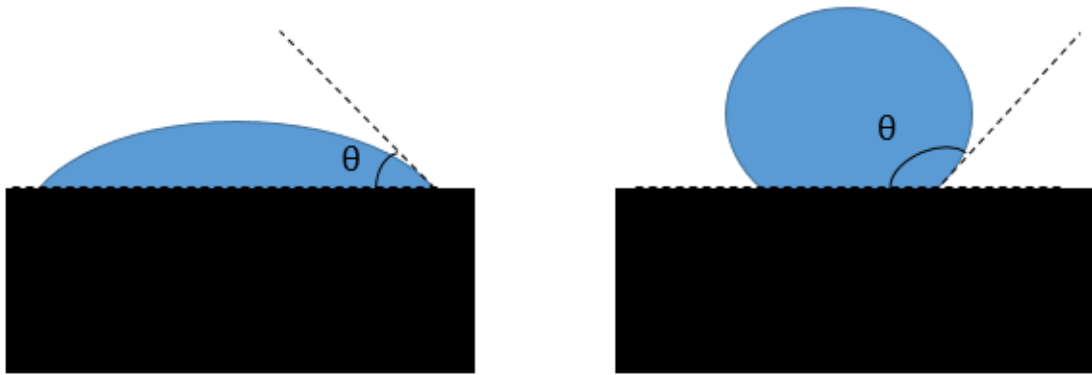


Figure 3-3. The contact angle measurement method.

3.2.3. Evaporation Suppression Chamber

A evaporation suppression chamber was build using aluminum alloy and glass slides, which were stabilized mechanically by copper wires in order to prevent the potential interaction with the liquid we used.

The top was covered with a clear polyester film, which was sealed to the glass slides. It also had a small hole to allow a syringe needle through to apply the drops to the fiber. The ends were covered with polyester triangles to limit evaporation in order to allow fiber holders go through the two ends. The size of the evaporation suppression chamber is $2 \times 0.5 \times 0.5$ inch. A schematic of the chamber is shown in Figure 3-4.

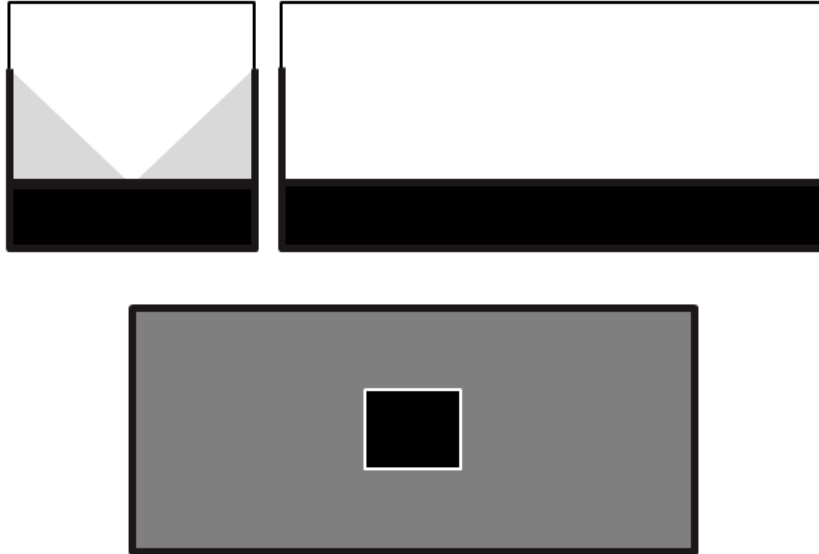


Figure 3-4. The three views of the evaporation suppression chamber: end, side, and top (The black is aluminum, the white color is the transparent glass, copper wire is applied to fasten the glass and the aluminum part together, and grey is a transparent polyester film).

3.2.4. Microliter Droplet Observation System

The microliter droplet observation system was built in lab, as shown in Figure 3-5. The evaporation suppression chamber was placed in front of the USB microscope, which is connected to the computer directly in order observe the wetting of the droplets. The USB microscope and the evaporation suppression chamber were connected firmly by a foam, which was cut to fit the cylindrical support of the USB microscope. Additional foam was cut to seal the ends of the evaporation suppression chamber. The video and images were obtained during the experiment and were recorded by the computer.

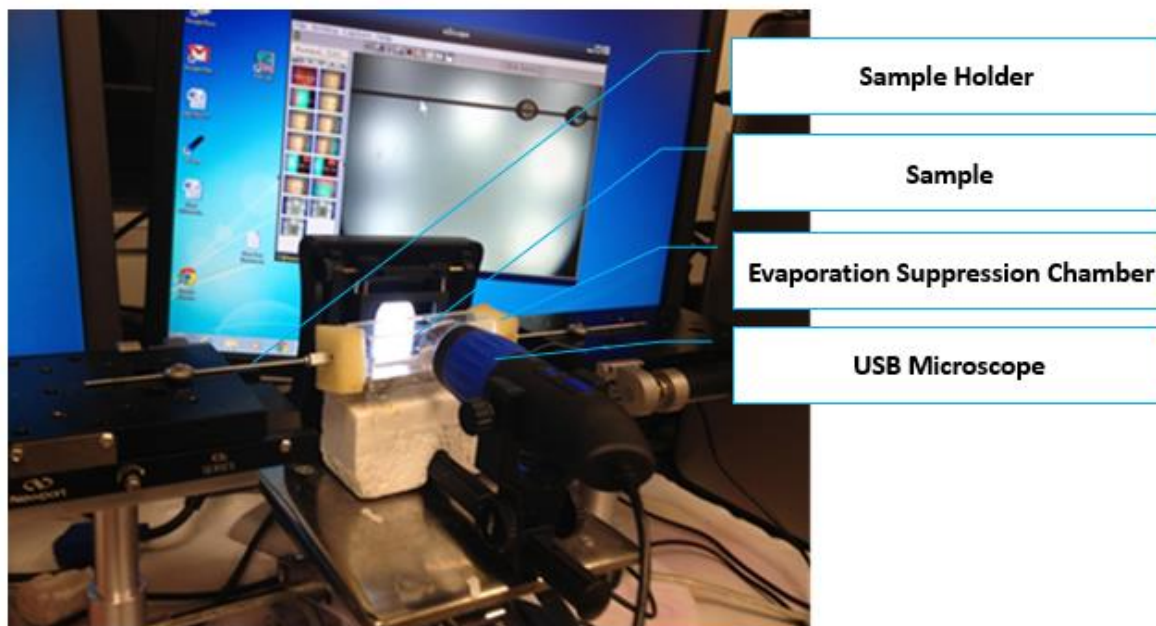


Figure 3-5. The improved measurement system showing the video-microscope in the foreground and the recorded image in the background. The chamber is in the middle.

3.2.5. Picoliter Droplet Observation System

The picoliter droplet observation system was built, as shown in Figure 3-6. The image of the picoliter liter droplets was captured by high-speed camera and delivered to the laptop. The light source illuminated the sample for image capture. The picoliter liter applicator generated droplets and delivered the drops through a picoliter syringe. The motion stage was used to adjust the position of the sample precisely.

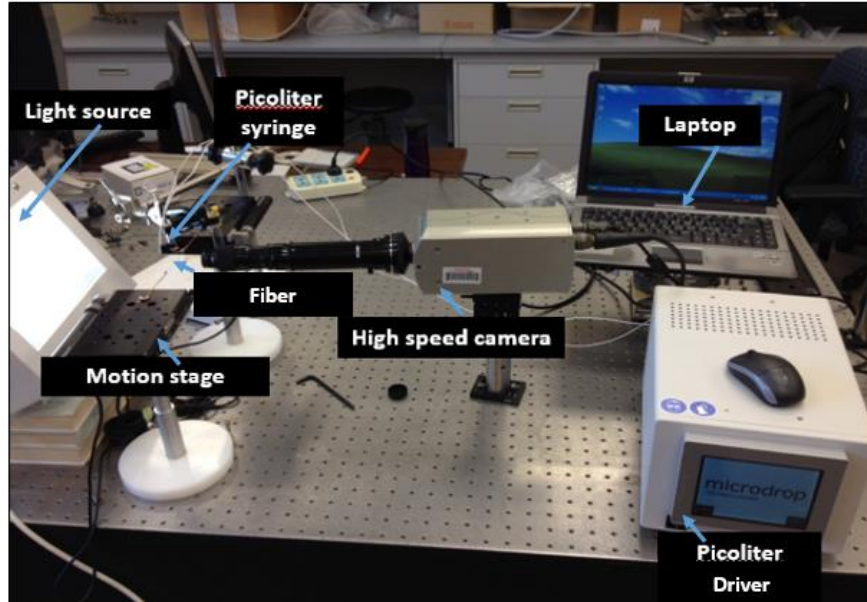


Figure 3-6. The apparatus for observation of picoliter droplets using a high-speed video camera.

Due to the small drop size, the system had to be very precise and stable. A close up of the stabilized system is in Figure 3-7. The fiber holder consisted of two nuts. By rotating the nuts on screws, the distance between the two nuts could be adjusted so the fiber could be tightened or loosened depending on our needs. At the same time, the two stages were mounted firmly on the vibration isolation table.

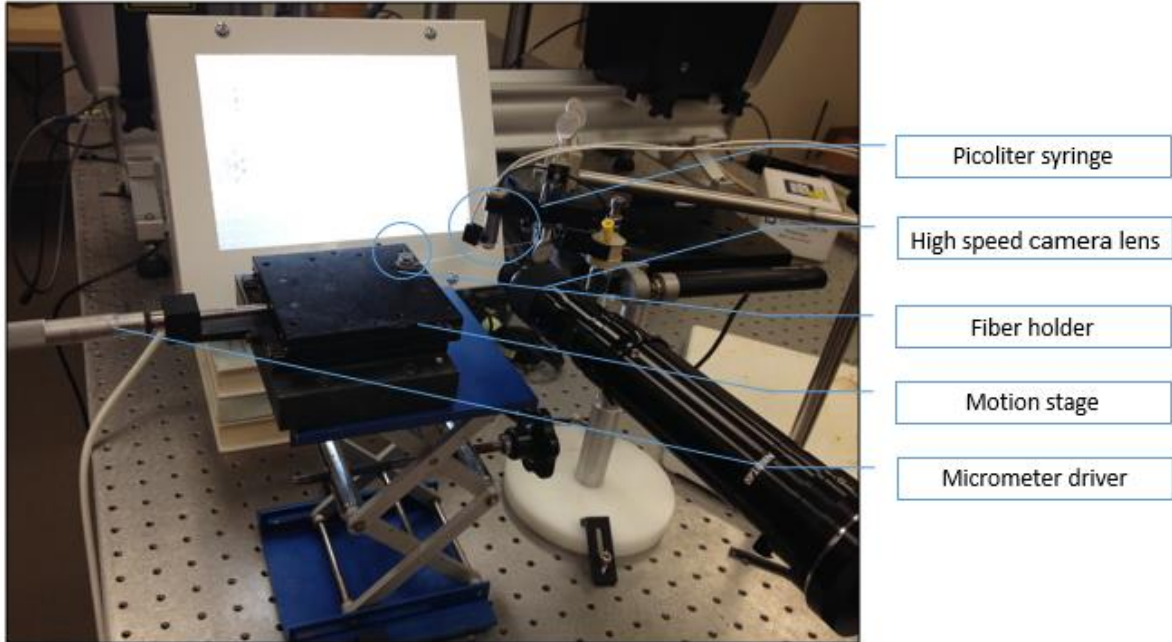


Figure 3-7. The details of the fiber sample stabilization system.

3.3. Structure Formation

3.3.1. Formation of flat smooth surface

Flat surfaces made from PMMA, wax, and indium were prepared separately but in a similar way. A glass slide was placed on a hot plate. PMMA, wax, or indium beads were melted on a glass slide respectively. When the beads melted, a cold slide was placed on top of the melted beads, which created a smooth surface. In this way, flat surfaces of PMMA, wax, and indium were created.

3.3.2. Formation of fibers

PMMA fibers were produced in lab by stretching molten PMMA beads using two tweezers. By adjusting the rate of the stretch, fibers with smooth surface or grooved surface can be produced. When the stretch was applied at high temperature using a high rate stretching, the fiber tended to be very smooth. When the stretch was applied at a relatively low temperature, the fiber tended to form grooves on the surface of the fiber.

3.3.3. Formation of Cones

Indium is a unique metal that can be melted at 156.6 °C. Indium cones with smooth surfaces were prepared by pulling molten indium rapidly using two tweezers, which resulted in two indium cones with smooth surfaces.

3.3.4. Formation of Spindle Knot Fiber

In order to create spindle knot on fiber surfaces, UV photo polymerization was used. A resin solution was prepared by dissolving 10 wt % poly(methyl methacrylate), PMMA, in methyl methacrylate, MMA, and 0.5 wt % Irgacure 379 was added as an initiator. A fiber was dipped into this solution and then removed from the solution. Due to the Rayleigh instability, the thin coating on the fiber surface broke into equally distributed droplets, which were solidified immediately at room temperature by UV light. The polymerized beads were gently pushed together in order to control the distance between them. The procedure is shown in Figure 3-8. Wax spindle knots were created in the same way but without the polymerization since they could be solidified by cooling to room temperature.

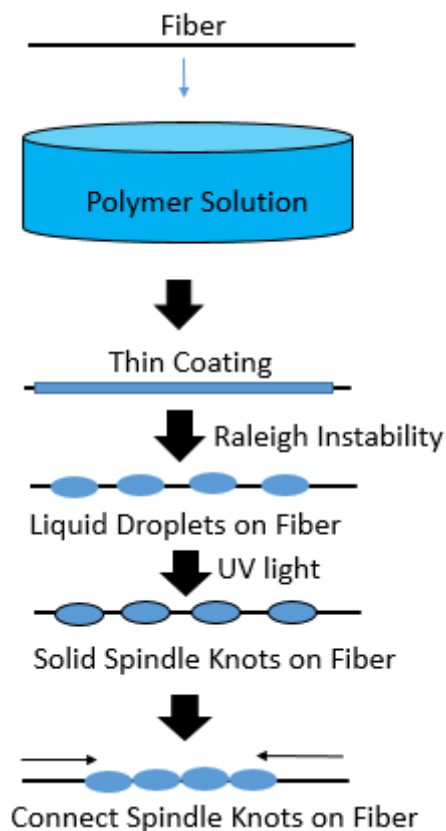


Figure 3-8. The production of spindle knot fiber through UV photo polymerization.

3.4. Surface Modification

PMMA spindle knot fibers and PMMA flat surfaces were coated by wax and HFTT respectively. The surface modified spindle knot fiber and flat surface were prepared by immersing prepared sample into wax or HFTT solution and pulling out gradually. A thin coating of wax or HFTT was applied evenly on the surface of the PMMA spindle knot. After drying in hood for 3 hours, the thin layer was dry enough to use.

3.5. Wetting Behavior of Droplet on Flat Surface

3.5.1. Microliter droplet on flat surface

Flat surfaces coated with indium, PMMA, wax and HFTT, respectively, were prepared. The contact angle of water, glycerol, dodecane and Kaydol (surface tension given in Table 3-1, which is based on the MSDS offered by the manufacture) were measured 5 times at different locations on the treated flat surface.

Table 3-1. The surface tension of liquids used.

Liquid	Surface Tension (mN/m)
Water	72
Glycerol	64
Kaydol	32
Dodecane	25

3.5.2. Picoliter droplet on flat surface

Dodecane picoliter droplets were generated by picoliter applicator and applied to PMMA flat surface. The parameters of the picoliter droplet applicator are listed in Table 3-2.

Table 3-2. The parameters of picoliter droplet applicator.

<i>Item</i>	<i>Value</i>
Voltage/(V)	120
Pulsewidth/(μ s)	11
Frequency/(Hz)	10

The control parameters of the high-speed camera are listed in Table 3-3.

Table 3-3. The parameters of high speed camera.

<i>Resolution</i>	800*600
Sample rate	1200
Exposure	600
Post trigger	2191

The profile of the microliter droplets was observed through picoliter droplet observation system.

3.6. Droplet Profile

3.6.1. Microliter Droplet on cylindrical fiber

Before the start of each experiment, the performance of the evaporation suppression system was verified. The microliter droplet observation system was then used to monitor the collection and growth of microliter drops generated in mist mode. A single polypropylene monofilament with diameter of 0.406 mm was placed in the chamber. Water aerosol drops were applied using a perfume atomizer multiple times. The coalescence of droplets was observed using the microscope.

3.6.2. Picoliter Droplet on cylindrical fiber

Dodecane picoliter droplets were generated and applied to the cylindrical fiber with diameter of 30 micrometers. At the same time, the droplet was observed using the picoliter droplet observation system. The control parameters of the picoliter applicator and the high-speed cameras were the same as in Table 3-2 and Table 3-3.

3.7. Droplet Coalescence

3.7.1. Microliter Droplet on yarns

Spandex yarn was used as the yarn in this experiment. The structure of the spandex yarn was observed using SEM. A spandex yarn was mounted between the two motor driven stages in the microliter droplet observation system described in the section 3.2.4 and stretched. Then, microliter water drops were placed on the yarn at a small separation distance. The time required for the drops to merge was recorded from the recorded video.

In addition, a web from a local Basilica spider was collected and examined. The web was photographed in the early morning and dew can be seen on the web. The structure of the spider silk was observed using an optical microscope. At the same time, the behavior of water droplets sprayed by a sprayer on the same spider silk in droplet mode was observed using the microscope.

3.7.2. Picoliter Droplet on grooved Fiber

Dodecane picoliter droplets were generated and applied to the grooved cylinder PMMA fiber with diameter of 200 micrometer. At the same time, the droplet was observed using the

picoliter droplet observation system. The control parameters of the picoliter applicator and the high-speed cameras were same as in Table 3-2 and Table 3-3.

3.8. Droplet Motion

3.8.1. Microliter shape droplet on spindle knot

Spindle knots with different surfaces and sizes were selected as the substrates to observe the motion direction of the four listed microliter droplets with volume of 0.1 and 0.5 microliter, as shown in Table 3-1. The spindle knots information was listed in Table 3-4. Droplets were applied to the spindle knots by microliter syringe. The wetting behavior of the droplets was observed using the microliter droplet observation system.

Table 3-4. The label indicating the spindle knot used and the shape parameters of the spindle knots.

<i>Label†</i>	<i>Surface</i>	<i>Cone Half Angle (°)</i>	<i>Fiber Diameter D (μm)</i>	<i>Maximum Width W (μm)</i>	<i>Length (μm)</i>
P-16	PMMA	15.7	228	578	1465
P-21		21	216	679	1820
P-20		20	228	771	1728
W-29	Wax	29	216	864	1777
W-26		26	216	1142	2191
W-27		26.9	216	1123	2148
F-19	HFTT	19.3	241	731	1759
F-17		17	224	730	1866
F-22		22	224	628	1365

3.8.2. Picoliter shape droplet on spindle knot

Dodecane picoliter droplets were generated and applied to the PMMA spindle knot fiber with diameter of 30 micrometer. At the same time, the wetting behavior of droplets was observed using the picoliter droplet observation system. The control parameters of the picoliter applicator and the high-speed cameras were same as in Table 3-2 and Table 3-3.

3.8.3. Clamshell Shape Droplet on Cone

The profile of a 1.0 μL clamshell droplet of water, glycerol and Kaydol, were observed on indium cones using USB microscope through the microliter droplet observation system.

Meanwhile, wetting behavior of water droplets with volume of 0.1 microliter on indium cones and picoliter sized drops on PMMA beads were observed using the same system.

4. RESULTS AND DISCUSSION

4.1. Droplet on Flat Surface

4.1.1. Microliter Droplet on Flat Surface

When droplets with different surface tensions were deposited on surfaces with different surface tensions, different profiles were formed, as shown in Figure 4-1 .

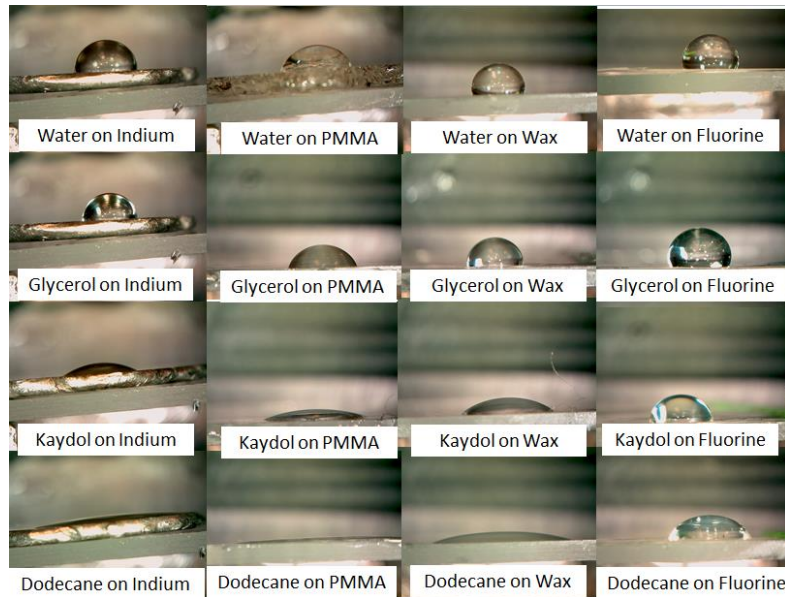


Figure 4-1. The droplet profile of different liquids on different flat surfaces (“Fluorine” refers to a fluorosilanated surface, see text.).

Young’s contact angle was used to characterize these different profiles, as shown in Table 4-1. From the value of the contact angle, it is not hard to find that for the same type of droplet, the higher surface energy surface lead to a lower contact angle. Meanwhile, for the same

surface, higher surface tension leads to higher contact angle. The data listed in the table shows a wide range of surface tensions of liquids and solids. The number of the surface tension was given in the MSDS of the material.

Table 4-1. Contact angles of different droplets on flat surfaces.

<i>Liquid</i>	<i>Water</i>	<i>Glycerol</i>	<i>Kaydol</i>	<i>Dodecane</i>
<i>Surface</i>	$\gamma_{LV} = 72$ <i>mN/m</i>	$\gamma_{LV} = 64$ <i>mN/m</i>	$\gamma_{LV} = 32$ <i>mN/m</i>	$\gamma_{LV} = 25$ <i>mN/m</i>
Indium $\gamma_{SV} = 560$ mN/m	$105.6 \pm 3^\circ$	$95.6 \pm 2.8^\circ$	$12.7 \pm 3.1^\circ$	$5.8 \pm 0.8^\circ$
PMMA $\gamma_{SV} = 42.5$ mN/m	$73.3 \pm 1.7^\circ$	$70.8 \pm 2.5^\circ$	$11.5 \pm 1.7^\circ$	$7.8 \pm 0.7^\circ$
Wax $\gamma_{SV} = 32$ mN/m	$102.1 \pm 2.2^\circ$	$97.6 \pm 2.1^\circ$	$45.6 \pm 2.1^\circ$	$21.7 \pm 1.6^\circ$
Triethoxyheptadeca fluoro-silane $\gamma_{SV} = 17.2$ mN/m	$118.6 \pm 2.8^\circ$	$112.2 \pm 4.8^\circ$	$94.4 \pm 6.7^\circ$	$66 \pm 4^\circ$

4.1.2. Picoliter Droplet on Flat Surface

The contact angle measurement mentioned above is based on droplet with volume of 10 μL . In aerosol mist, the droplets are much smaller than that. Picoliter level droplets were generated and applied to a PMMA surface. The profiles of the droplets with increasing volume were observed through high-speed camera. According to the observation, the picoliter droplet behaves the same as the microliter droplet. As shown in Figure 4-2, the contact angle for dodecane is still around 7.5, which is the same as at 10 μL level. These three pictures were taken during 1.82 seconds with a total number of 18 drops of picoliter size droplet with a diameter around 50 μm . Therefore, we concluded that wetting behavior of picoliter droplets behave same as microliter droplet on flat surface.

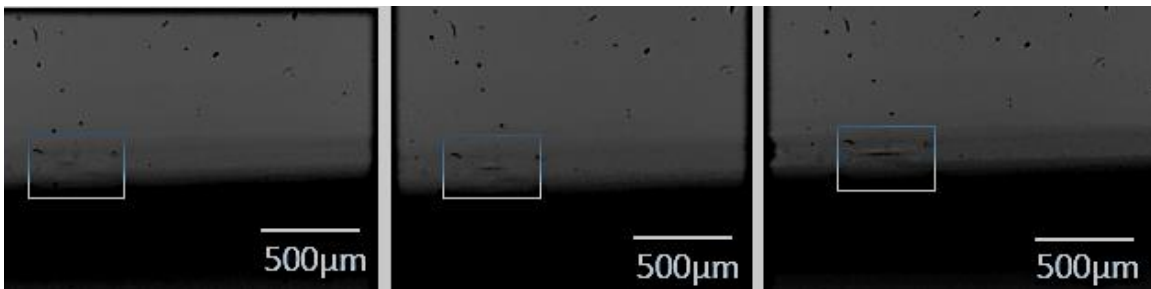


Figure 4-2. The dodecane droplet growth on PMMA flat surface.

4.2. Droplet on Single Fiber

When substrate surface is not flat, the droplet will form a different three-dimensional profile from the one on a flat surface in order to maintain the balance of the liquid molecules on the

contact line along the local surface. In this study, the profiles of the droplets on cylindrical fiber, conical fiber, and spindle knot fiber have been studied.

4.2.1. Droplet on Cylindrical Fiber

Water droplets were deposited on a polypropylene fiber using a mist sprayer, as shown in Figure 4-3.

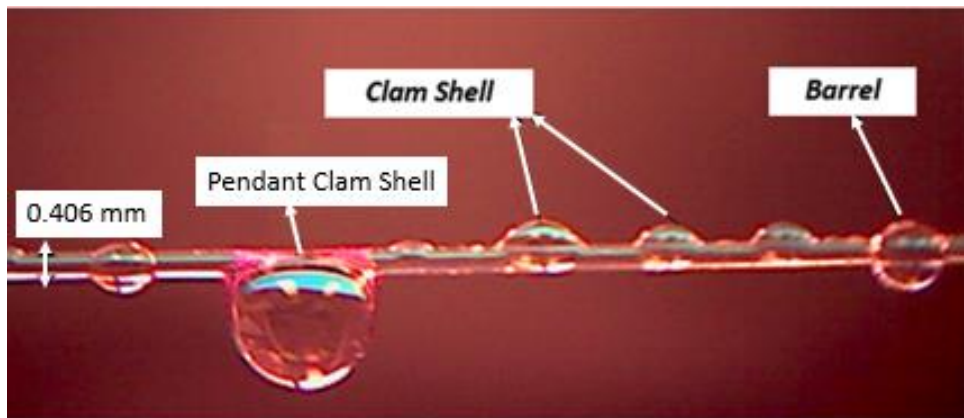


Figure 4-3. Barrel shape and clam-shell shape profiles on PP fiber.

As we can see from Figure 4-3, the droplets with different profiles were formed on fiber. In this study, droplets are classified as clamshell shape droplet and barrel shape droplet. The profiles of clamshell shape droplet and barrel shape droplets will be discussed in the following paragraphs.

4.2.1.1. Barrel Shaped Droplet on Cylindrical Fiber

Profile of the droplet on cylindrical fiber has been mathematically calculated with known contact angle, fiber diameter, and droplet volume, as described in the section 2.4.4.

4.2.1.2. Clamshell Shaped Droplet on Cylindrical Fiber

Profile of clamshell shaped droplet has been studied using surface evolver simulation, as reviewed in the section 2.4.4. At the same time, the transition point from clamshell to barrel shape droplet has been determined the by the ratio of droplet volume to fiber diameter⁶⁷.

4.2.1.3. Droplet Growth on Cylindrical Fiber

These studies of static droplets give us the shape information for a single droplet sitting on the surface. In order to understand the collection process of the small droplets from air, the droplet growth on fiber under mist mode and droplet mode has been studied in this study.

Picoliter water droplets were deposited on a PMMA fiber with diameter of 30 μm , as shown in Figure 4-4. The growth process of the water droplet with increasing volume of the droplet is shown in Figure 4-4 at picoliter level under droplet mode. However, for aerosol mist, the droplets not only hit a single point but hit the entire surface of the fiber.

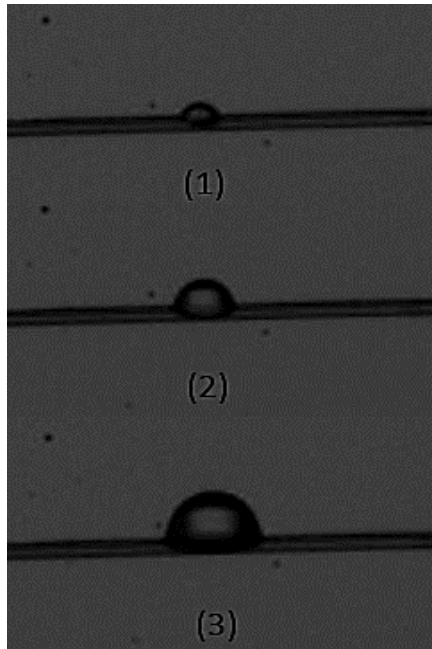


Figure 4-4. Water growth on PMMA smooth fiber under droplet mode (Fiber Diameter is $30\ \mu\text{m}$).

In mist mode, the water droplets were widely deposited on the surface, as shown in Figure 4-5. We can see that as the density of the droplets gets higher as the deposition time increases. At the same time, discrete droplets were formed on the fiber, which is same as the result shown in Figure 4-4.

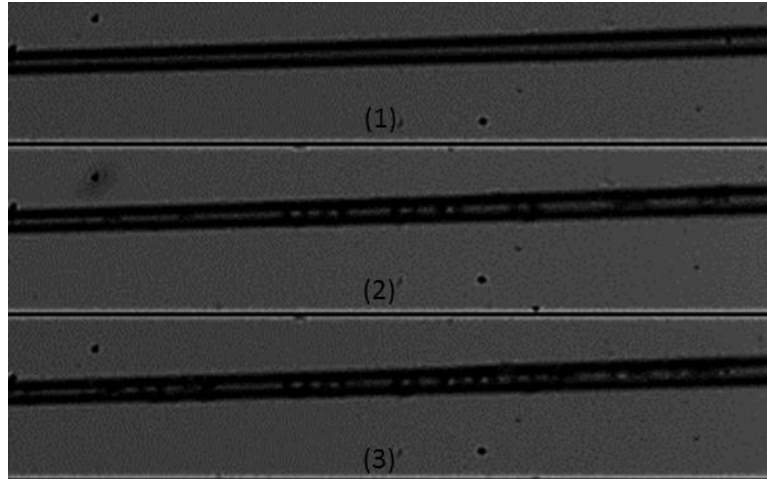


Figure 4-5. Water droplet on PMMA smooth fiber under mist mode (Fiber Diameter is $30\mu\text{m}$).

Based on Figure 4-4 and Figure 4-5, we can see the distribution of the droplets by mist mode and the growth of the droplets by droplet mode. Water droplets can form obvious discrete droplets on PMMA fiber.

Dodecane droplets were also deposited on the same fiber under both droplet mode and mist mode, as shown in Figure 4-6 and Figure 4-7 respectively. Both figures do not show discrete droplets on the fiber, which is very different from the water droplets on smooth PMMA surface.

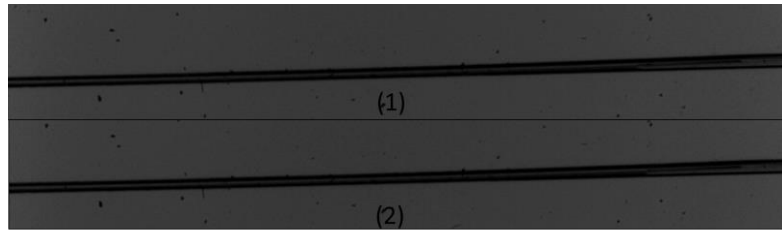


Figure 4-6. Dodecane on smooth PMMA fiber under droplet mode.

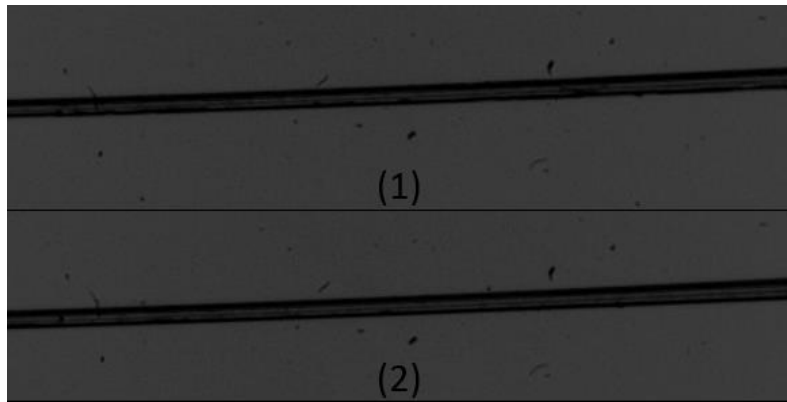


Figure 4-7. Dodecane on smooth PMMA fiber under mist mode.

It is not hard to explain the wetting behavior of aerosol dodecane droplets on PMMA fiber using its contact angle on flat surface. As we can see, the contact angle of water on PMMA flat surface is 73° . However, the contact angle of dodecane on PMMA flat surface is 7.5° . For a droplet with a small contact angle, it is much easier to spread on fiber surface instead of forming a discrete droplet, especially on a fiber with a small diameter. At the same time, the

smaller contact angle leads to smaller average molecular distance between the liquid and the solid. Therefore, the capillarity, which is caused by the molecular attraction between the solid and liquid interface, is higher for smaller contact angles due to the high attraction force between liquid and liquid molecular force. It strengthens the spreading of the liquid molecules on the fiber surface.

For small droplets on fiber surface, we conclude that it is easier for droplets with higher contact angle to form discreet clamshell droplets, while it is easier for droplets with lower contact angle spread on fiber surface.

Under mist mode, the growth of the droplets can be classified by two approaches. The first approach is the direct collection of the tiny droplets from air, namely the mist. The second approach is the merging of the two nearby droplets when they physically touch or are connected by a small droplet deposited between them. With the gathering of the droplets under mist mode, the droplets grow to bigger droplets until transformation from clamshell shape to barrel shape occurred. Barrel shape can continuously increase in volume until gravity starts to dominate the profile of the droplet. Finally, the pendent clamshell droplet is formed, which is easy to get off from the fiber when the whole system is out of balance. The process is observed using a microscope and demonstrated in Figure 4-8.

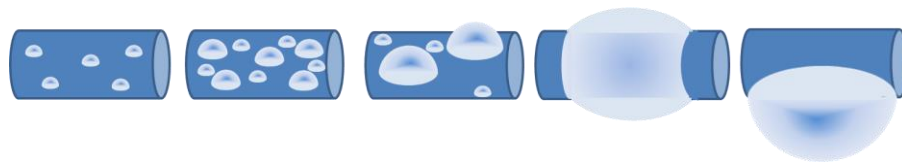


Figure 4-8. A schematic of the growth process of droplets on a fiber.

At the same time, it is notable that all droplets grow randomly, which means the barrel shape and clamshell shape can appear at the same time, as shown in Figure 4-3. Therefore, for following study, both types of droplets will be discussed.

4.2.2. Droplet on Conical Fiber

4.2.2.1. Barrel Shaped Drop on a Conical Fiber

The profile of barrel shape droplets has been studied, as described in section 2.4.5. At the same time, the Gibb free energy of the droplet on cone surface has been demonstrated, which indicated that the barrel shape droplet will move to the lowest Gibbs free energy location on the cone. However, this study only focused on barrel shape droplet, which is just one type of the droplets on the fibers.

4.2.2.2. Clamshell Shaped droplet on Conical Fiber

Profiles of clamshell shaped droplets on a conical fiber were simulated using Surface Evolver[®] and experimentally verified. Profiles of 1 μL droplets, including water, glycerol, and Kaydol, from simulation and experiment were compared as shown in Figure 4-9, Figure 4-10 and Figure 4-11.

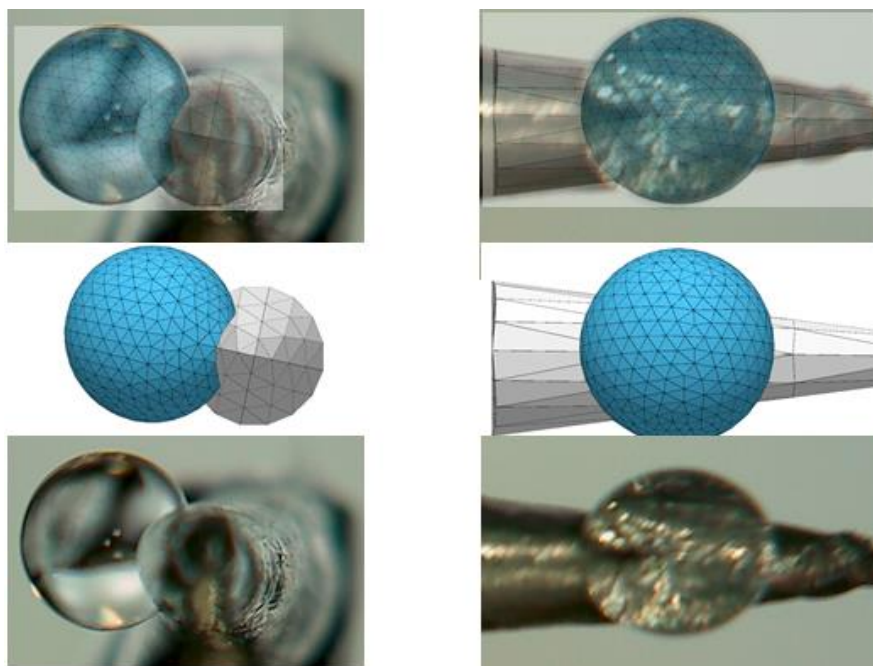


Figure 4-9. Comparison of the shape of the 1 μL water droplet based on simulation and experiment.

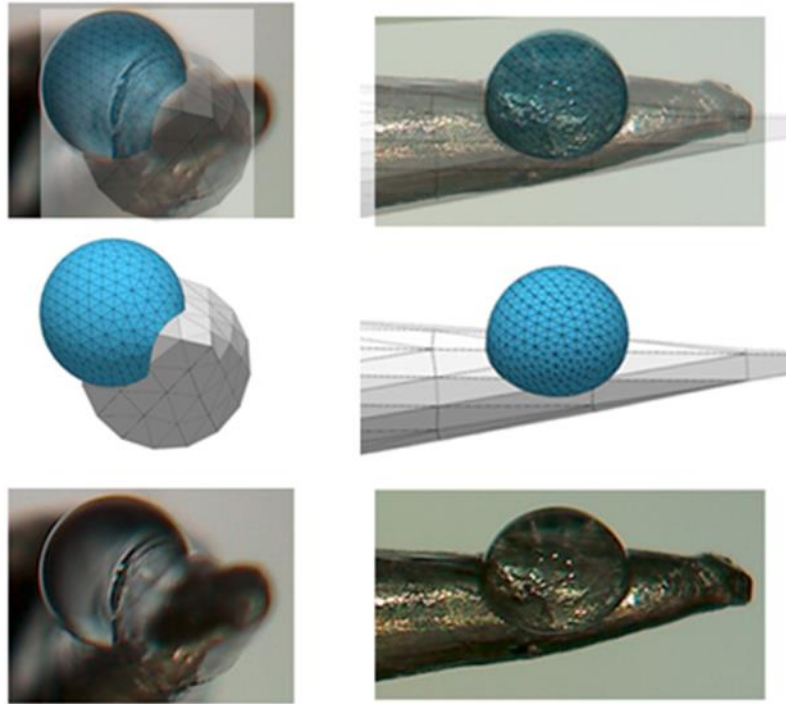


Figure 4-10. Comparison of the shape of the 1 μL glycerol droplet based on simulation and experiment.

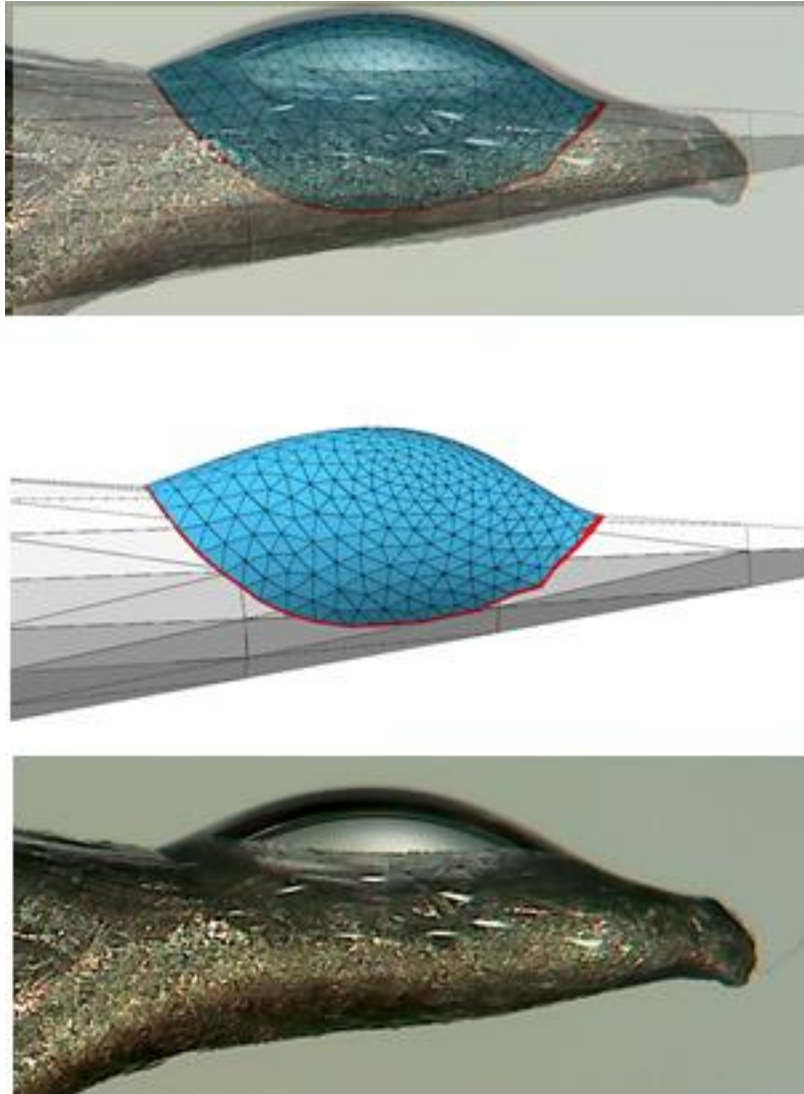


Figure 4-11. Comparison of the shape of the 1 μL Kaydol droplet based on simulation and experiment.

High consistency between the profiles obtained based on theory calculation and experiment has been achieved. To further answer the question whether the clamshells droplet will move to the widest part of the cone, experiments have been conducted, as shown in Figure 4-12.

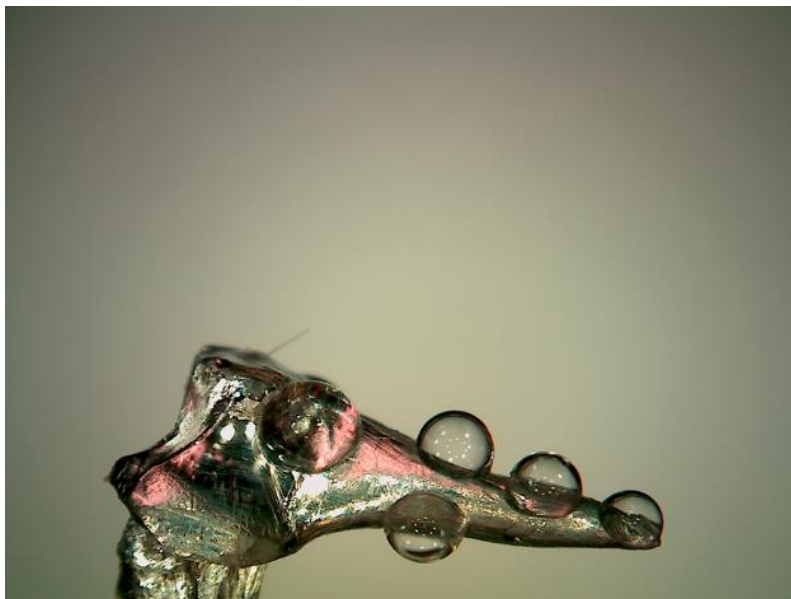


Figure 4-12. 0.1 μL water droplets on indium cone (cone angle is 14° and length of the widest part is $1214 \mu\text{m}$).

According to observation, the clamshell droplets on cones don't move spontaneously. They always stayed where they were deposited. This result conflicts with the statement made in the section 2.4.5. The wetting behavior of clamshell can also be interpreted using theory. On a spindle knot, clamshell droplet and the solid are two systems that are relatively separated from each other. In other way, the Gibbs free energy of the droplet surface can be maintained at the minimal level by changing the surface area of the droplet, which can be obtained by expanding the droplets along the axis or diameter direction. However, for barrel shaped droplet, to obtain the lowest Gibbs free energy, the droplet has to change its surface area by moving the droplets along the axis direction because the other direction has been occupied by

its self. Therefore, we conclude that clamshell shaped droplets won't spontaneously move on spindle knots.

4.2.2.3. Droplet Growth on Conical Fiber

Based on result above, barrel droplets will move to the lowest Gibbs free energy point on the cone. Clamshell droplets will stay where they are deposited. Therefore, there will be two approaches for droplet growth on conical fiber. Firstly, droplets can growth through collecting droplets from mist. Secondly, droplets can growth through physically touching nearby droplets. Unlike passive physical touching between two droplets, two droplets on cones may touch because of the directional motion of the barrel shape under certain conditions. Therefore, a cone can speed up the growth of the droplet by moving a barrel shape droplet spontaneously.

To utilize the droplet collection properties of the cone in fibers, spindle knot structures were designed in order to be more feasible in final applications, as shown in Figure 4-13. The wetting behavior of droplets on spindle knot will be discussed in the next section.

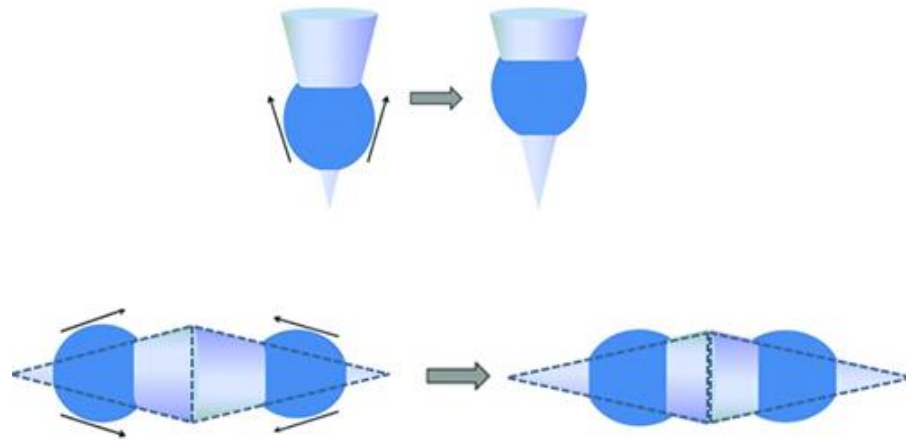


Figure 4-13. The relationship between cone and spindle knots.

4.2.3. Droplet on Spindle Knot Fiber

4.2.3.1. Barrel Shape on Single Spindle Knot

Based on the method developed by Michielsen et al, the Gibbs free energy of droplet on spindle knot has been mathematically calculated based on the model shown in Figure 4-14.

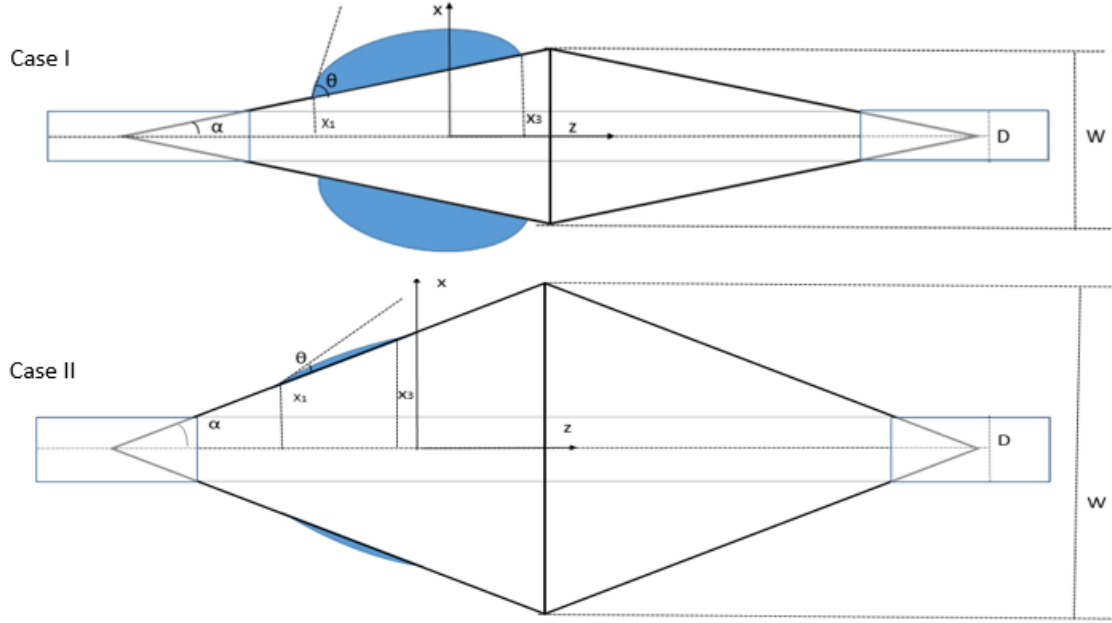


Figure 4-14. Illustration of parameters and boundary conditions in case I and case II (D is the fiber diameter, W is the maximum width of the spindle knots, α and θ are the half cone angle and contact angle of the droplet on spindle knot surface).

On a spindle knot, the Gibbs free energy of the droplet on the cone can be written as

$$G_s = \gamma_{SV} \frac{\pi W(W-D)}{4 \sin \alpha} + \gamma_{LV} \left\{ 2\pi x_2 [a_I x_1 + x_2] E(\varphi_I, k_I) + S(a_{II} x_3 + x_2) E(\varphi_{II}, K) - \frac{\pi}{\sin \alpha} (x_3^2 - x_1^2) \cos \theta \right\} \quad 4.1$$

where γ_{SV} is surface tension between air and the cone surface, γ_{LV} is surface tension between the liquid and its vapor, a_I and a_{II} are variable substitutions. $E(\varphi_I, k_I)$ and $E(\varphi_{II}, k_{II})$ are elliptical integrals of the second kind. S defines the sign appropriate for the case.

Compared with the Gibbs free energy of the droplet on cone, three modifications are needed to extend this analysis to the case of spindle knots. First, the minimum value for x_1 (horizontal ordinate of one end) is D , the fiber radius. Second, the maximum value of x_3 (horizontal ordinate of the other end) is just the widest radius of the spindle knot, W . Third, the drop may remain on one side of the spindle knots, or it may straddle the widest region. If the drop remains on one side of the maximum width or the other, this state could be the equilibrium state, or a metastable state since the same value of x_1 and x_3 occur on both sides of the widest region.

The trend of Gibbs free energy of droplets with different volume on different surfaces in the range of $D/2$ to $W/2$ were obtained using Matlab. At the same time, the final equilibrium locations were observed. The comparison between theory and experimental is listed in Table 4-2.

Table 4-2. The final location of the liquid drops on the spindle knots from the theoretical calculations and from experiments

<i>Volume</i> (μL)	<i>Spindle Knot</i>	<i>Liquid</i>	<i>Final drop location</i> [†]	
			Theory	Experiment
0.1	P-21	glycerol	N	N
	P-16	Kaydol	W	W
	P-21	Kaydol	W	W
	P-20	Kaydol	W	W

Table 4-2 Continued.

	P-16	dodecane	W	W
	P-21	dodecane	W	W
	P-20	dodecane	W	W
	W-29	water	N	N
	W-26	water	N	N
	W-29	Kaydol	N	N
	W-26	Kaydol	N	N
	W-27	Kaydol	N	N
	W-29	dodecane	W	W
	W-26	dodecane	W	W
	W-27	dodecane	W	W
	F-19	water	N	N
	F-17	water	N	N
	F-22	water	N	N
	F-19	glycerol	N	N
	F-17	glycerol	N	N
	F-22	glycerol	N	N
	F-19	Kaydol	N	N
	F-17	Kaydol	N	N
	F-19	dodecane	N	N
	F-22	dodecane	N	N
0.5	P-16	glycerol	N	N
	P-21	glycerol	N	N
	P-20	glycerol	N	N
	P-16	Kaydol	W	W

Table 4-2 Continued.

P-21	Kaydol	W	W
P-20	Kaydol	W	W
P-16	dodecane	W	W
P-21	dodecane	W	W
P-20	dodecane	W	W
W-29	Kaydol	N	N
W-26	Kaydol	N	N
W-27	Kaydol	N	N
W-29	dodecane	W	W
W-26	dodecane	W	W
W-27	dodecane	W	W
F-19	Kaydol	N	N
F-17	Kaydol	N	N
F-22	Kaydol	N	N
F-19	dodecane	N	N
F-17	dodecane	N	N
F-22	dodecane	N	N

†The drop location is N for the narrowest region and W for the widest region.

There are 27 out of 72 groups of samples and liquid that cannot form barrel shapes on the spindle knot fibers, as shown in Figure 4-15, which will not be considered as the theoretical predictions are only valid when the drop has the barrel shape.

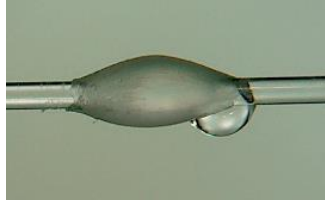


Figure 4-15. A water clamshell droplet on a spindle knot fiber (0.1-water-P-21)

For the other samples, experimental results agree with the theory study, as summarized in *Table 4-3*.

Table 4-3 The comparison between theory and experiment in terms of number of groups at each equilibrium location

<i>Position</i>	<i>Theory</i>	<i>Experiment</i>
Narrowest	50	27
Clamshell	N/A	27
Widest	22	18
Total	72	72

Based on the data listed in these tables, there is good agreement between the experimental data and the theoretical results when the barrel shaped drop occurs. Due to space limitation, two examples were used to describe the situation of the droplet moving to the widest part and to the narrowest part separately. Representatives of the two different results are shown in

Figure 4-16 and Figure 4-17 separately. Figure 4-16 shows a droplet that moved spontaneously to the widest part of the spindle knot. Figure 4-17 is the case for the droplet that remained where it was deposited, i.e. the narrowest part of the spindle knot.

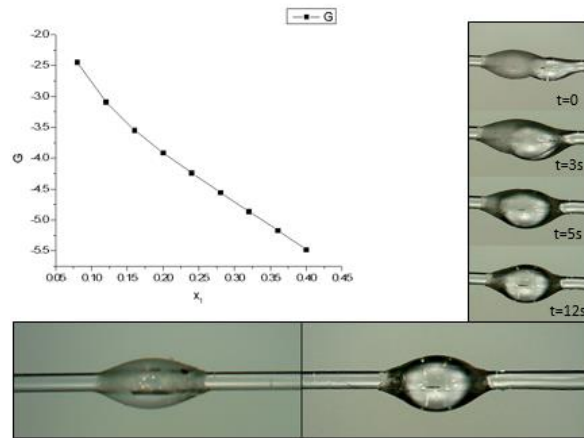


Figure 4-16. The theoretical study of the Gibbs energy trend and the experimental verification (0.1-Dodecane-P-20).

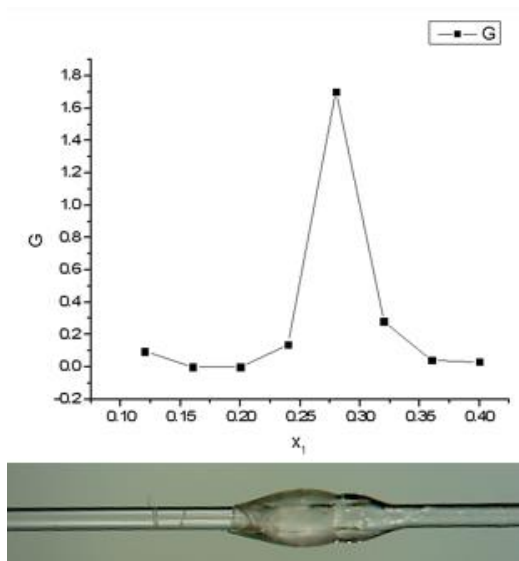


Figure 4-17. The theoretical study of the Gibbs free energy and the experimental verification of location (0.1-dodecane-F-19).

From the result above, the motion of the barrel shape on spindle knots has been interpreted well using lowest Gibbs free energy theory. Based on the result, to make the droplet move spontaneously, it has to be the proper combination of shape of the spindle knot and contact angle of the liquid on the spindle knot. The dodecane droplet on PMMA surfaces will move to the widest part spontaneously at different half cone angle of the PMMA spindle knots. The same phenomenon was observed in the picoliter observation system for dodecane droplets on PMMA spindle knot fiber, as shown in Figure 4-18.

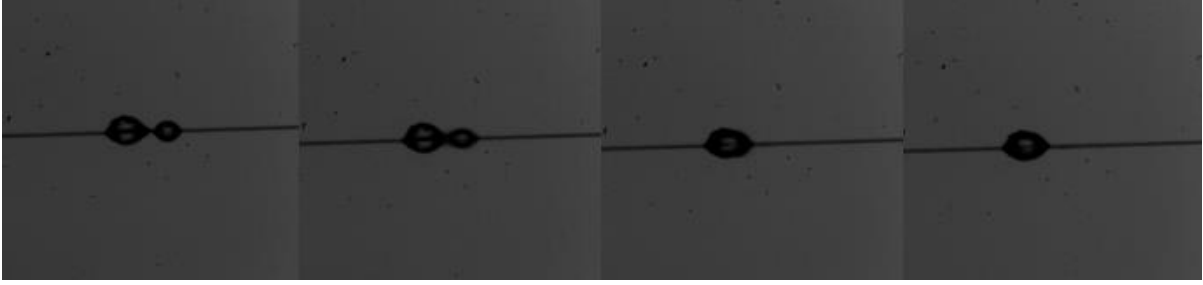


Figure 4-18. Dodecane droplet on PMMA single fiber

From the high speed camera system, we can see that the time used for the droplet to move to the widest part of the cone is about 0.8 ms. This figure indicates that for droplets with a much smaller volume than microliter also move spontaneously on the designed PMMA spindle knots.

4.2.3.2. Clamshell Shaped Droplet on Single Spindle Knot

Microliter size clamshell droplets were observed in the previous section, which didn't move on spindle knot. The wetting behavior of clamshell droplet at picoliter level also has been observed, as shown in Figure 4-19 and Figure 4-20. Neither the smaller droplet in the figure nor the bigger droplet moved on the bi-cone structure. The smaller droplet is a single droplet generated by picoliter applicator, which has the diameter of 50 μm . We conclude that both microliter and picoliter clamshells don't move on spindle knots.

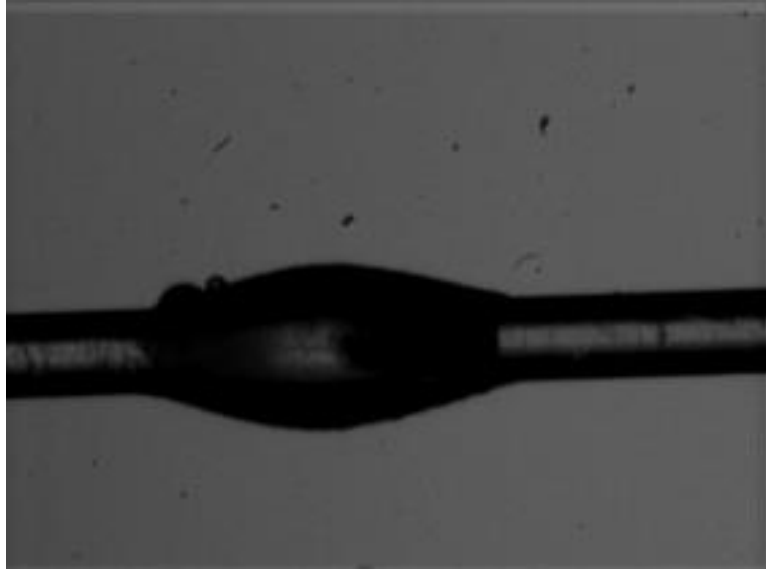


Figure 4-19. Water clamshell droplet on PMMA single spindle knot fiber (fiber diameter is 450 μm).

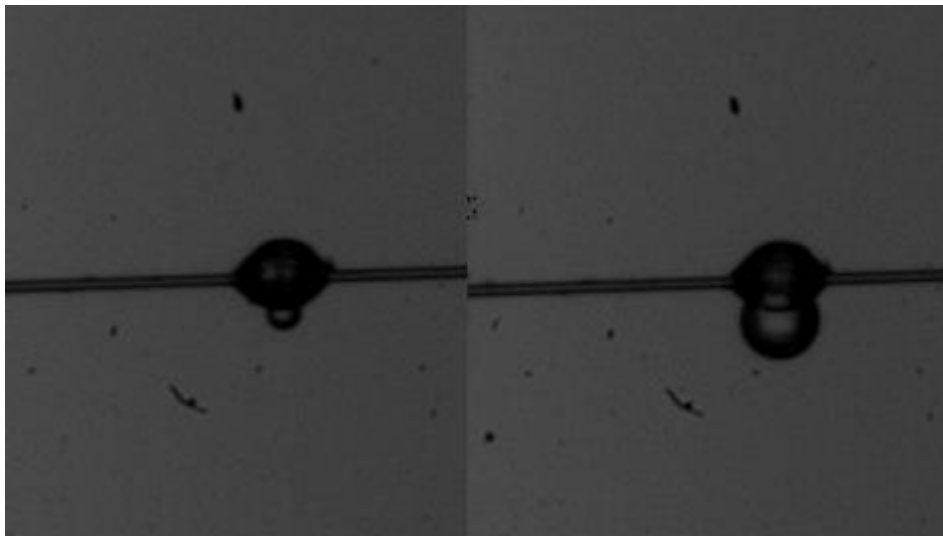


Figure 4-20. Water clamshell droplet on PMMA single spindle knot (fiber diameter 30 μm).

4.2.3.3. Small Droplet Collection on Connected Spindle Knot Fiber

Connect spindle knots were used to collect picoliter dodecane and water droplet under droplet mode, as shown in Figure 4-21 and Figure 4-22.

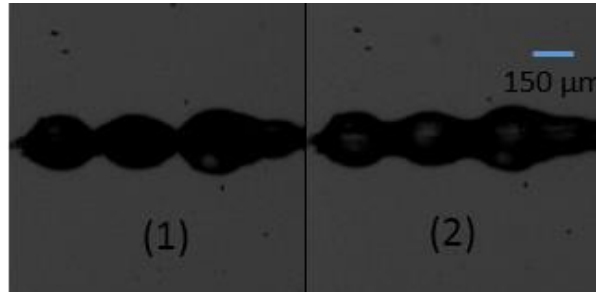


Figure 4-21. Dodecane droplet collection on connected spindle knots under mist mode.

In Figure 4-21, (1) shows the figure of the spindle knot before spraying. (2) shows the appearance of the fiber covered by dodecane. Dodecane droplet under the mist mode will cover the entire spindle knot surface with a larger thickness increase at the narrowest part. Until the narrowest regions were filled with liquid, the liquid in each valley combined together and formed a big droplet due to Rayleigh instability, as shown in Figure 4-22.

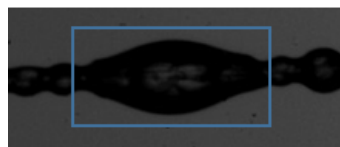


Figure 4-22. Dodecane droplet on spindle knot after collection.

When we connect these spindle knots, it is hard to obtain a barrel shape droplet directly due to the small volume of the droplets. Therefore, clamshell shape is the most common droplet profiles on connected spindle knots in mist mode. When we spray dodecane onto the spindle knot, they stay where they were due to the properties of clamshell. However, with continuous spraying, some liquid will move to the narrowest part of the spindle knot pushed by a force caused by the collision between the existing droplets and following droplets due to the spraying direction and relative high velocity of each drops when contacting with the spindle knot surface. Therefore, the thickness of the widest part will be thinner than that at the narrowest part.

At the same time, the wetting behavior of water droplets on connected spindle knots are shown in Figure 4-23 ((1) is the PMMA spindle knot before spraying. (2) is the PMMA spindle knot after spraying) and Figure 4-24. In both figures, droplets formed discrete droplets without expanding on connected spindle knots. Both figures indicates that connected spindle knots do not help the growth of clamshell shaped water droplets. To collect those discrete droplets, some structure is necessary to speed up the formation of the barrel shape droplet.

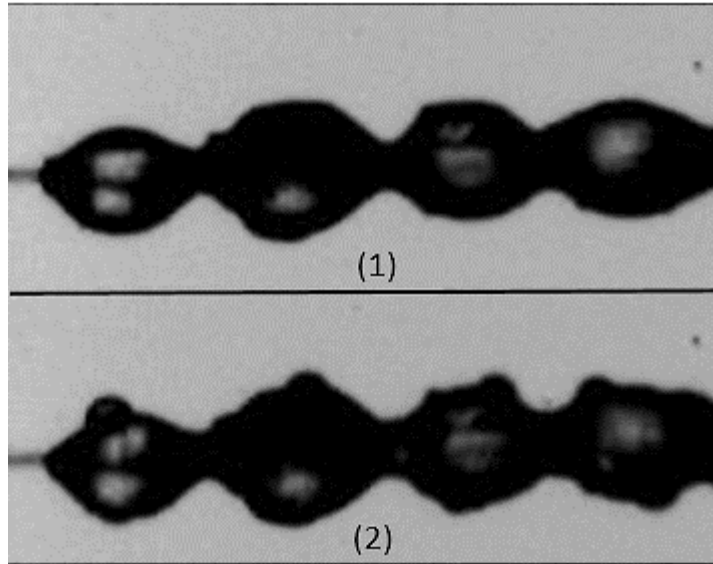


Figure 4-23. Water spray on connected spindle knots (describe left and right).

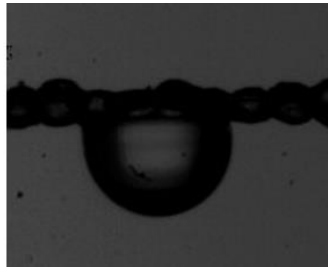


Figure 4-24. Water droplets on spindle knot fiber.

Based on this section, there are two requirements to speed up the collection. First, the size and surface tension of the spindle knots has to be properly designed. Second, the droplets on the spindle knots have to be in the shape of barrel shape instead of clamshell shape. By connecting these spindle knots together, the highest cone area was obtained. However, the

area for the droplet transformation was sacrificed, which lead to only a small portion of droplets that can be moved directionally because all other droplets remained in the clamshell shape. Therefore, an area for droplets to transform should be left between two spindle knots.

4.3. Droplet on Multifilament Yarn

To connect two spindle knots, a single or multiple filaments can be used. The droplet behavior on single smooth fiber has been studied in section 4.2.1. In this section, we will discuss the wetting behavior of droplets on multifilament yarn.

4.3.1. Capillarity on Grooved Fibers

PMMA grooved fiber was made in order to observe if the grooves on the fiber surfaces will change the wetting behavior of the droplets on fiber surfaces.

Figure 4-25 to Figure 4-28 show picoliter droplets on PMMA grooved fiber. From these figures, we can conclude that a dodecane droplet won't form a discreet droplet on a PMMA groove fiber. However, a water droplet will form discreet droplets on PMMA grooved fiber. However, the volume of the droplet was decreased, as shown in (2) and (3) in Figure 4-26, which is caused by the capillarity produced by the grooves on PMMA fiber. By comparing with the result for droplet on PMMA smooth fiber, as shown in section 4.2.1, we concluded that the grooves on the fiber surfaces increase the capillarity of these drops and help them move along these micro channels.

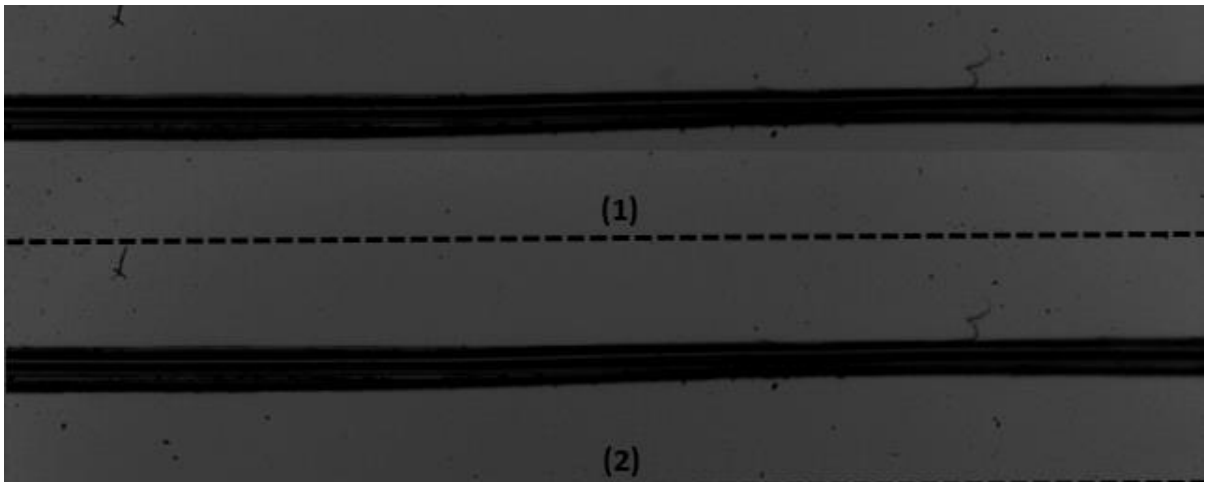


Figure 4-25. Dodecane drops on grooved fiber (fiber diameter 200 nm).

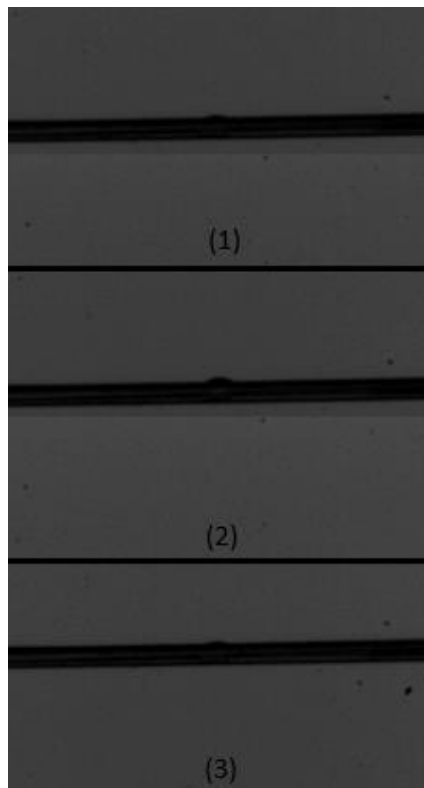


Figure 4-26. Water drops on grooved fiber (fiber diameter 200 nm).

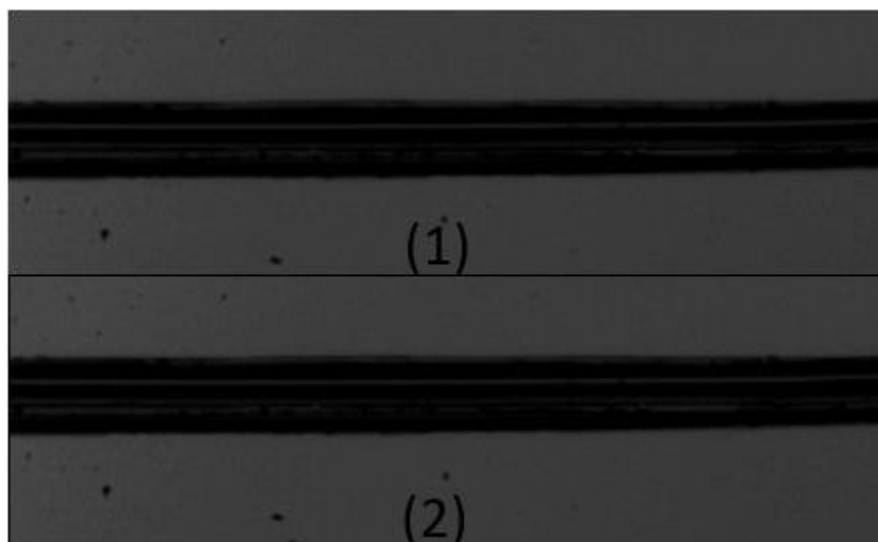


Figure 4-27. Dodecane spray on grooved fiber (fiber diameter 200 μm).

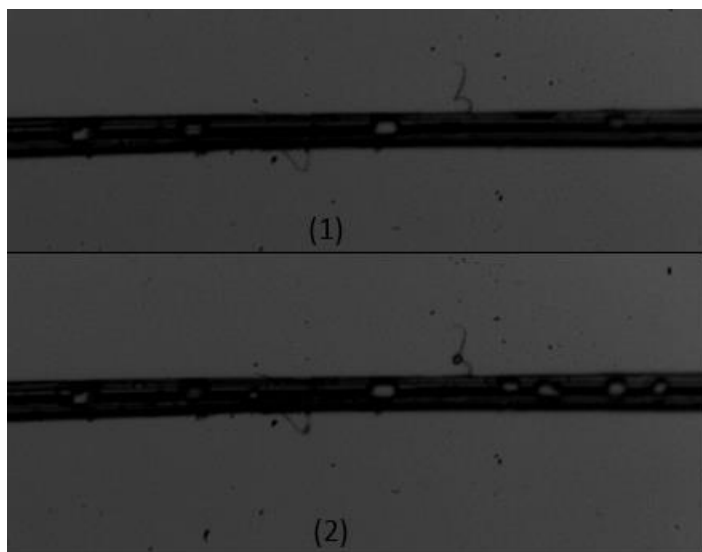


Figure 4-28. Water spray on grooved fiber (fiber diameter 200 μm).

From the comparison of the dodecane and water droplets on smooth fiber and on grooved fiber, it is observed that the dodecane droplet is easier to expand on grooved fiber compared with water droplet, which is easy to understand because water droplet has much higher contact angle on PMMA surface.

From the comparison of the water droplet on grooved fiber and on smooth fiber, it is obvious that water droplets on grooved fiber expand more easily on grooved fiber surface, as shown in Figure 4-26, from (2) to (3), which is caused by the capillarity caused by the grooves on fiber surface.

Therefore, to make the surface coalescence drops quickly, grooves on the fiber will generate capillarity of the substrate and enhance coalescence. In addition, covering the surface with many small droplets from a mist helps promote capillarity.

4.3.2. Droplet Coalescence on Multifilament Yarn

Yarn is composed of many fibers assembled into a bundle, which creates many channels for the motion of liquids. The SEM image of the unstretched spandex yarn with a diameter of 350 μm is shown in Figure 4-29. When it was stretched, its diameter is only around 30 μm . From the SEM image of the spandex yarn, we can see that there are many micro channels in the spandex yarns. The shape of the water droplet at different times is shown in Figure 4-30.



Figure 4-29. SEM image of the spandex used in the experiments described in the text.

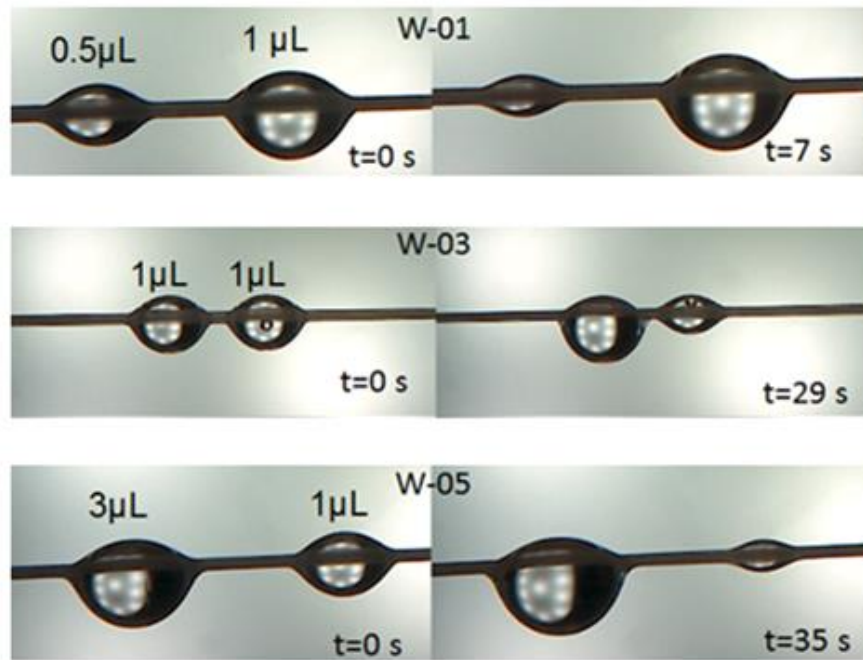


Figure 4-30. Merging of static water droplets on spandex yarn over time.

Figure 4-30 shows the pictures captured from the videos obtained during experiments. Each row shows the same two drops at time 0s and at a later time. Five groups of experiment were conducted but only three are shown. As we can see from each group, the smaller droplet was always consumed by the larger droplet.

The merging of droplets was driven by the difference between the droplets' Laplace pressures and resisted by the viscous flow of the liquid over the distance between the two droplets. The drop volumes, the distance between drops and the times to merge are listed in Table 4-4. V_1 is the volume of the smaller droplet. V_2 is the volume of the bigger droplet. L is

the distance between the two droplets as shown in the modeling section. The time used to totally merge the droplet is t .

Table 4-4 Experimental Drop Parameters for Several Coalescing Water Droplet Pairs

V_1 (μL)	V_2 (μL)	L (μm)	t (s)	L/t ($\mu\text{m/s}$)
0.5	1.0	891	10	89.1
0.5	4.0	1113	7	159
1.0	1.0	116	109	1.06
1.0	2.0	724	57	12.7
1.0	3.0	1050	44	23.8
1.0	5.0	1391	69	20.2

To better understand the coalescence between two droplets, a model was built for the merging of the two droplets, as shown in Figure 4-31. The yarn was composed of several cylindrical fibers. The two droplets sitting on the yarn were connected by liquid within yarns. The Laplace pressures of the two droplets were ΔP_1 and ΔP_2 , respectively. The droplets can be clamshell or barrel shape droplets as long as they are sitting on the yarn.

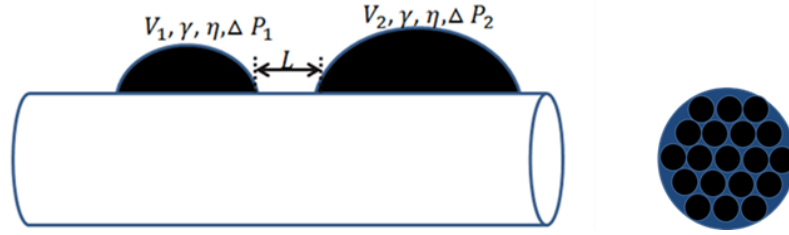


Figure 4-31. Microflow mode created for droplets on multifilament yarns.

This study analyzed the motion of micro flow after the two droplets connected through the channels in the yarn due to capillarity. The model is based on Hagen Poiseuille law and Laplace pressure. The derivation of the equations is given in the appendix. The final expression of the relationship between the time t and distance between the two droplets L is:

$$t = K \frac{\eta L}{\gamma_{LV}} \int_0^{V_1} \frac{dv}{\left[(V_1 - v)^{-1/3} - (V_2 + v)^{-1/3} \right]} = K' t L \quad 4.2$$

where t is the time taken for droplet 1 to merge with droplet 2, K is a shape factor that is only related to the morphology of the yarn, L is the distance between the droplets, η is the viscosity of the liquid from the two droplet, γ_{LV} is the liquid vapor surface tension, V_1 and V_2 are the volumes of the two droplets. From this equation, the relationship between the L and t is linear.

All the data obtained was plotted according to the final equation described in the experiment. The comparison of the modeling result and the experimental date is shown in Figure 4-32.

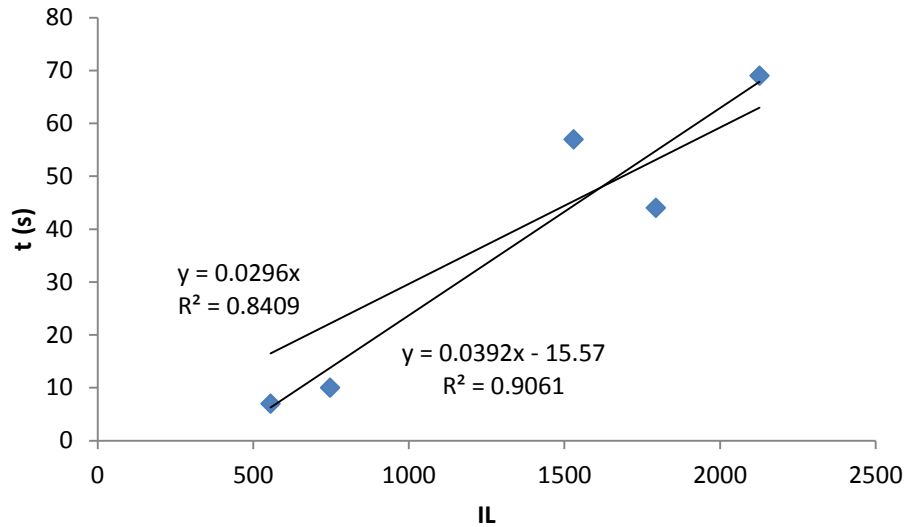


Figure 4-32. The time required for two drops to coalesce is shown versus the integrated term IL , the numerical intergral times the distance between the two droplets. (Heavy line is fit to equation, which the narrow line is best fit).

From Figure 4-32, two linear relationships were build according the data obtain in experiment. The heavy blue line is the trendline of the data passing through $(0, 0)$. The narrow black line is the best fit of the data using linear regression. The best fit line didn't pass through $(0,0)$, which may be explained in the following paragrah.

The volume of the droplet is measured by syring before depositing the droplet onto the spandex yarn. However, the time recorded for the merging process starts from the moment when the two droplets begain to decrease. Therefore, there is a time lag in our experiment which cannot be avoided.

This part of the research showed that capillarity and the Laplace pressure driven motion plays an important role in speeding up the water collection on spandex yarns. Capillarity is only present when there are microchannels. At the same time, to allow spreading the contact angle between the droplet and the material cannot be too high.

4.3.3. Droplet Coalescence on Spider Silk

We compared these results to similar experiments on a real spider web, as shown in Figure 4-33. The support yarns are composed of two parallel filaments that are not entangled with each other. The net yarns consist of at least two filaments that are twisted about each other. When water mist was sprayed onto the supporting filaments, the small droplets coalesced with the larger droplets in a very short time. This is similar to the behavior observed on the spandex yarn, see Figure 4-34.

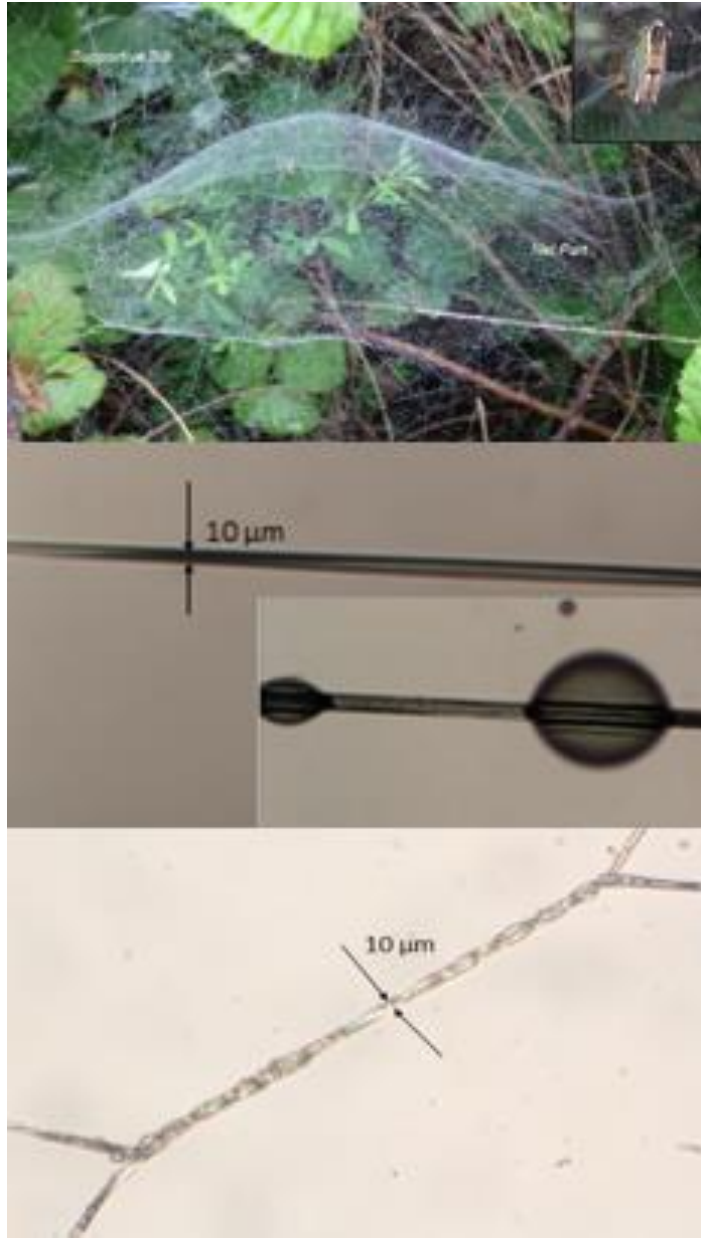


Figure 4-33. The web of a Basililca spider from Lake Raleigh, Raleigh, NC is shown along with the support structure and the net portion of the web.

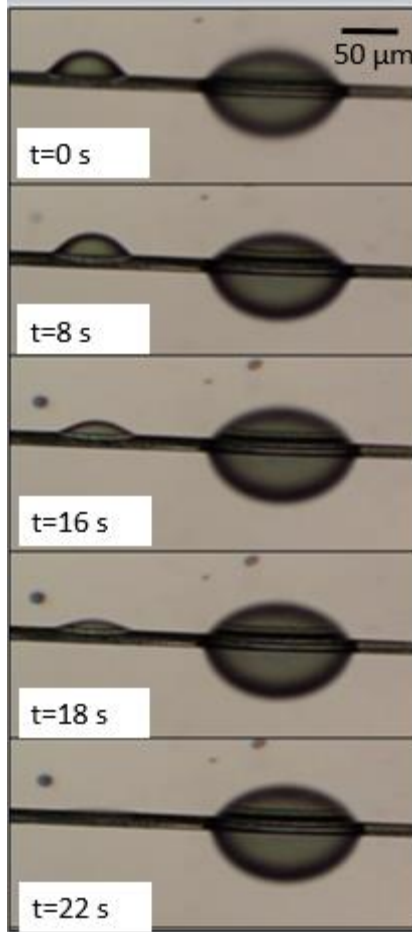


Figure 4-34. The coalescence of water droplet from mist on the support structure yarns from the web of a Basilica spider.

This analysis is consistent with the observation that spider webs collect water due to the capillarity caused by the channels or grooves on the yarn surface. It also indicates an important application of multifilament yarns. This conclusion will be used to design and produce the right fabric structure to speed up the water collection process.

4.4. Design of the Highly Efficient Aerosol Barrier

4.4.1. Design of the Yarn Structure

Based on the function of spindle knot and multifilament yarns, fiber structure was designed to collect liquid aerosols, as shown in Figure 4-35. In order to make full use of the capillarity and Gibbs free energy driven motion, a grooved monofilament or a multifilament yarn is used to create micro channels to assist capillary driven merging of nearby drops and spindle knots are applied in order to speed up the motion of barrel shape droplets that are close to the spindle knot. The size and surface tension of the spindle knot needs to be further designed according to the properties of the droplets. Based on the calculation of Gibbs free energy, the parameters that dominate the Gibbs free energy of the spindle knots are the contact angle between liquid and solid, the half cone angle of the spindle knot, and the volume of the droplet. In industrial application, the material of the spindle knot and the contact angle between the spindle knot material and the aerosol droplet is known. With known contact angle and droplet volume, we can calculate the Gibbs free energy trend through Matlab using a wide range of half cone angles. By observing the Gibbs free energy trends generated based on different half cone angles, the groups that can make droplet move spontaneously can be determined. In the end, the half cone angle of the spindle knots can be determined and engineered using technologies that can create spindle knots on fiber, such as Rayleigh instability and 3D printing.

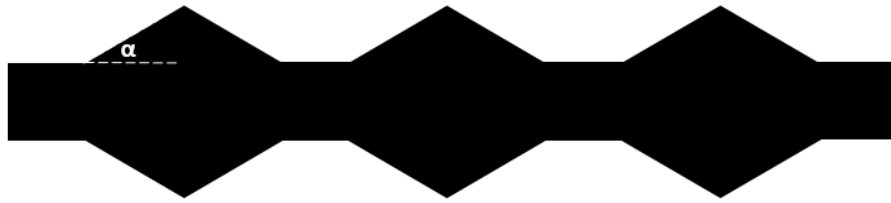


Figure 4-35. The designed fiber structure.

As we discussed, spindle knots only speed up the collection of the barrel shaped droplet. For clamshell droplets, multifilament yarn structure is necessary in order to help the collection. In this study, the yarn connecting the spindle knot can have different morphologies according to the industrial application as long as they have grooves on yarn to create possibilities for capillarity. Several examples have been demonstrated in Figure 4-36.

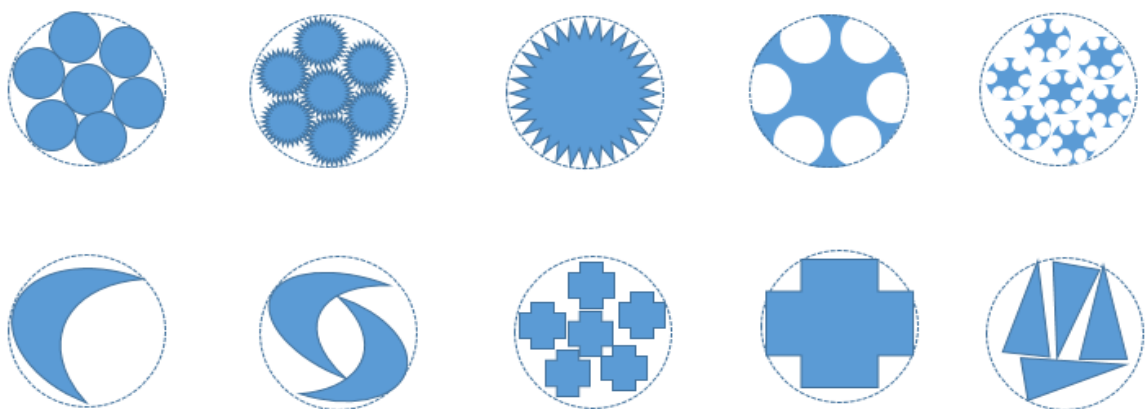


Figure 4-36. Possible yarn morphologies that could be used for this project.

4.4.2. Design of the Fabric Structure

The structure of the fabric structure was further designed, as depicted in

Figure 4-37. The three demos listed Figure 4-37 can be possible macrostructures used to set up the spindle knot fibers. Demo 1 is a plain woven structure with spindle knots on weft yarns. Demo 2 is another plain woven structure with spindle knots with increasing volume along the warp direction. Demo 3 is a nonwoven structure with spindle knots randomly distributed on fabrics.

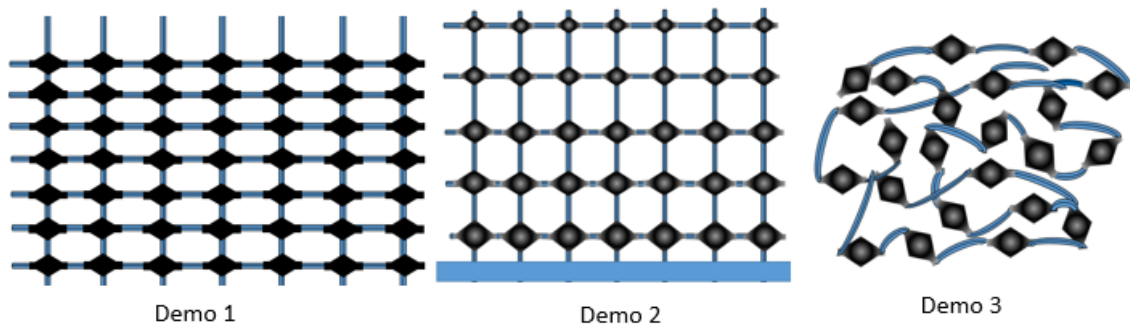


Figure 4-37. The possible fabric structures.

At the beginning of the spraying, the droplet will contact with the spindle knot part and the multifilament, which will build liquid bridges for following drops to merge with each other. Discreet drops will be formed with the spraying of the mist due to capillarity of the micro channels and Rayleigh instability. As the drops merge, they form barrel shaped droplets that

are connected to spindle knot through the capillary channels and move to the widest region of the spindle knots.

At the same time, droplets with different sizes on different spindle knots will merge with each other through the micro channels on the fibers that connect the adjacent spindle knots, which is driven by Laplace pressure differences among droplets. In this way, the aerosol droplets can be collected and transported directionally.

5. CONCLUSION

Through this study, wetting behavior of droplets including both barrel shape and clamshell shaped drops were studied on different surfaces with different surface tension. At the same time, microliter and picoliter droplets were carefully observed, including the capillarity, the pressure driven communication on yarn, and the spontaneous motion on spindle knots. These experimental and theoretical studies lead to the conclusions below;

1. To make a barrel shape droplet move spontaneously to the widest part of the spindle knot, the Gibbs free energy trend of the droplet on the cone has to be at its minimum at the widest part of the spindle knot, which requires the proper combination of the half cone angle of the spindle knot and the contact angle of the droplet on spindle knot surface. The calculation method has been explained in this study.
2. There is no way to make the clamshell droplet move spontaneously on smooth spindle knot fibers. However, clamshell drops can be moved by Laplace pressure difference if the droplet is connected to another droplet by the liquid in channels beneath the droplet.
3. In this study, droplets regardless of their shape didn't merge with each other except when they are connected through the liquid between them. It was found that the coalescence of the droplets can be characterized by volume of the two droplets, the distance between them and the properties of the liquid using Hagen Poiseuille law.
4. The two known reasons that lead to the collection of the aerosol droplets on spider web is the droplet merging through multifilament structure and the spindle knot structure on the spider silk.

5. This study can be widely used in aerosol collection, filtration, and fog harvesting when certain parameters, including the half cone angle and the surface tension of the spindle knot, are applied according to the properties of the droplet, which indicates a very reliable promising solution for air purification, exhaust recycling, and water harvesting.

6. FUTURE STUDY

Firstly, the effect of surface texture on spindle knots can be studied in order to investigate if some texture can help spindle knots to collect and move droplets faster.

Secondly, the performance of other volatile liquids on spindle knots yarn can be studied. A structure that can collect liquid faster compared with the evaporation rate would be desired in many applications.

Thirdly, spindle knots fiber made of regenerated protein and cellulose is very promising to design and fabricate in the direction of water collection.

Fourthly, collection of mixture of liquid with different surface tension through spindle knots is a very interesting topic.

Fifthly, it is very interesting to study if some standard designed cones with scale can be used to measure the surface tension of the liquid in droplets according to the final equilibrium location on cones for droplets with certain volume. Compared with contact angle, this method will be easier to obtain the numbers without using extra equipment during experiment.

Lastly, the wetting behavior of droplets in another liquid atmosphere, which is immiscible with the liquid in the droplets, is very interesting to study. The findings can be used to look for new solutions for oil and water separation process.

REFERENCES

- (1) Zheng, Y., Gao, X., and Jiang, L. (2007) Directional adhesion of superhydrophobic butterfly wings. *Soft Matter* 3, 178.
- (2) Hou, Y., Chen, Y., Xue, Y., Wang, L., Zheng, Y., and Jiang, L. (2012) Stronger water hanging ability and higher water collection efficiency of bioinspired fiber with multi-gradient and multi-scale spindle knots. *Soft Matter* 8, 11236.
- (3) Bai, H., Ju, J., Sun, R., Chen, Y., Zheng, Y., and Jiang, L. (2011) Controlled fabrication and water collection ability of bioinspired artificial spider silks. *Adv. Mater.* 23, 3708–11.
- (4) Zheng, Y., Bai, H., Huang, Z., Tian, X., Nie, F.-Q., Zhao, Y., Zhai, J., and Jiang, L. (2010) Directional water collection on wetted spider silk. *Nature* 463, 640–3.
- (5) Li, K., Ju, J., Xue, Z., Ma, J., Feng, L., Gao, S., and Jiang, L. (2013) Structured cone arrays for continuous and effective collection of micron-sized oil droplets from water. *Nat. Commun.* 4, 2276.
- (6) Michielsen, S., Zhang, J., Du, J., and Lee, H. J. (2011) Gibbs free energy of liquid drops on conical fibers. *Langmuir* 27, 11867–72.
- (7) Carroll, B. . (1976) The accurate measurement of contact angle, phase contact areas, drop volume, and Laplace excess pressure in drop-on-fiber systems. *J. Colloid Interface Sci.* 57, 488–495.
- (8) Ko, F. K., Kawabata, S., Inoue, M., Niwa, M., Fossey, S., and Song, J. W. (2011) Engineering Properties of Spider Silk. *MRS Proc.* 702, U1.4.1.
- (9) Seidel, A., Liivak, O., Calve, S., Adaska, J., Ji, G., Yang, Z., Grubb, D., Zax, D. B., and Jelinski, L. W. (2000) Regenerated Spider Silk: Processing, Properties, and Structure. *Macromolecules* 33, 775–780.
- (10) Kluge, J. a, Rabotyagova, O., Leisk, G. G., and Kaplan, D. L. (2008) Spider silks and their applications. *Trends Biotechnol.* 26, 244–51.
- (11) Vepari, C., and Kaplan, D. L. (2007) Silk as a Biomaterial. *Prog. Polym. Sci.* 32, 991–1007.
- (12) Hinman, M. B., Jones, J. a, and Lewis, R. V. (2000) Synthetic spider silk: a modular fiber. *Trends Biotechnol.* 18, 374–9.

- (13) Hsia, Y., Gnesa, E., Pacheco, R., Kohler, K., Jeffery, F., and Vierra, C. (2012) Synthetic spider silk production on a laboratory scale. *J. Vis. Exp.* e4191.
- (14) Bai, H., Tian, X., Zheng, Y., Ju, J., Zhao, Y., and Jiang, L. (2010) Direction controlled driving of tiny water drops on bioinspired artificial spider silks. *Adv. Mater.* 22, 5521–5.
- (15) Dorsey, N. E. (1926) Measurement of surface tension, pp 563–595.
- (16) Marchand, A., Weijs, J. H., Snoeijer, J. H., and Andreotti, B. (2011) Why is surface tension a force parallel to the interface? *Am. J. Phys.* 79, 999.
- (17) Allan F. M, B. (1983) Handbook of solubility parameters and other cohesion parameters.
- (18) Adamson, A., and Gast, A. (1997) Physical Chemistry of Surfaces.
- (19) MacKeen, P. C., Person, S., Warner, S. C., Snipes, W., and Stevens, S. E. (1987) Silver-coated nylon fiber as an antibacterial agent. *Antimicrob. Agents Chemother.* 31, 93–9.
- (20) Feng, L., Zhang, Z., Mai, Z., Ma, Y., Liu, B., Jiang, L., and Zhu, D. (2004) A Super-Hydrophobic and Super-Oleophilic Coating Mesh Film for the Separation of Oil and Water. *Angew. Chemie* 116, 2046–2048.
- (21) Cerkez, I., Kocer, H. B., Worley, S. D., Broughton, R. M., and Huang, T. S. (2011) Multifunctional Cotton Fabric : Antimicrobial and Durable Press.
- (22) Treatment, P. (2010) Antistatic Property of Polyacrylonitrile Fiber by. *Text. Res. J.*
- (23) Du, Z., Cheng, X., and Huang, F. (2011) Research and Characterization of Water and Oil Repellent Finishing Auto Interior Materials. *Adv. Mater. Res.* 242, 837–842.
- (24) Sherrill, J., Michielsen, S., and Stojiljkovic, I. (2003) Grafting of light-activated antimicrobial materials to nylon films. *J. Polym. Sci. Part A Polym. Chem.* 41, 41–47.
- (25) Zhao, J., Shi, Q., Luan, S., Song, L., Yang, H., Shi, H., Jin, J., Li, X., Yin, J., and Stagnaro, P. (2011) Improved biocompatibility and antifouling property of polypropylene non-woven fabric membrane by surface grafting zwitterionic polymer. *J. Memb. Sci.* 369, 5–12.
- (26) Atrp, S. A. (2011) Hydrophobic Modification of Natural Cellulose Fiber with MMA via. *Mater. Res.* 221, 90–94.

- (27) Rachini, A., Troedec, M. Le, and Peyratout, C. (2012) Chemical Modification of Hemp Fibers by Silane Coupling Agents. *Polymer (Guildf)*. 123, 601–610.
- (28) Jia, Z., and Yang, Y. G. (2011) Structure and Properties of Soybean Milk Modified Polyacrylonitrile Fiber. *Adv. Mater. Res.* 204-210, 1295–1298.
- (29) Ehlert, G. J., Lin, Y., and Sodano, H. A. (2011) Carboxyl functionalization of carbon fibers through a grafting reaction that preserves fiber tensile strength. *Carbon N. Y.* 49, 4246–4255.
- (30) Antoni, P., Carlmark, A., Lindqvist, J., Emma, O., Hult, A., and Malmstro, E. (2009) Superhydrophobic and Self-Cleaning Bio-Fiber Surfaces via ATRP and Subsequent Postfunctionalization "I.
- (31) Tobiesen, F. A., and Michielsen, S. (2002) Method for grafting poly(acrylic acid) onto nylon 6,6 using amine end groups on nylon surface. *J. Polym. Sci. Part A Polym. Chem.* 40, 719–728.
- (32) Young, T. (1805) An essay on the cohesion of fluids. *Philos. Trans. R. Soc.*
- (33) Wenzel, R. (1936) Resistance of solid surfaces to wetting by water. *Ind. Eng. Chem.* 988–994.
- (34) Cassie, A., and Baxter, S. (1944) Wettability of porous surfaces. *Trans. Faraday Soc.* 546–551.
- (35) Gao, L., and McCarthy, T. J. (2007) How Wenzel and cassie were wrong. *Langmuir* 23, 3762–5.
- (36) Panchagnula, M., and Vedantam, S. (2007) Comment on how Wenzel and Cassie were wrong by Gao and McCarthy. *Langmuir* 225–226.
- (37) Kamath, Y. K., Hornby, S. B., Weigmann, H.-D., and Wilde, M. F. (1994) Wicking of Spin Finishes and Related Liquids into Continuous Filament Yarns. *Text. Res. J.* 64, 33–40.
- (38) Sadat, M., Jad, M., Abdolkarim, S., and Ravandi, H. (2011) Wicking Phenomenon in Polyacrylonitrile Nanofiber Yarn 12, 801–807.
- (39) Chen, X., Kornev, K. G., Kamath, Y. K., and Neimark, a. V. (2001) The Wicking Kinetics of Liquid Droplets into Yarns. *Text. Res. J.* 71, 862–869.
- (40) Kissa, E. (1988) Wetting Wicking 16, 215–222.

- (41) Kissa, E. (1996) Wetting and Wicking. *Text. Res. J.* 66, 660–668.
- (42) Taylor, P., Nyoni, A. B., and Brook, D. (2010) Wicking mechanisms in yarns — the key to fabric wicking performance Wicking mechanisms in yarns – the key to fabric wicking performance 37–41.
- (43) Perwuelz, A., Casetta, M., and Caze, C. (2001) Liquid organisation during capillary rise in yarns -influence of yarn torsion. *Polym. Test.* 20, 553–561.
- (44) Washburn, E. (1921) The dynamics of capillary flow. *Phys. Rev.*
- (45) Kawase, T., Sekoguchi, S., Fuj, T., and Minagawa, M. (1986) Spreading of Liquids in Textile Assemblies: Part I: Capillary Spreading of Liquids. *Text. Res. J.* 56, 409–414.
- (46) Hollies, N. R. S., Kaessinger, M. M., Watson, B. S., and Bogaty, H. (1957) Water Transport Mechanisms in Textile Materials: Part II: Capillary-Type Penetration in Yarns and Fabrics. *Text. Res. J.* 27, 8–13.
- (47) Weilin, Q., Mala, G. M., and Dongqing, L. (2000) Pressure-driven water flows in trapezoidal silicon microchannels 43.
- (48) Davey, N., and Neild, A. (2011) Pressure-driven flow in open fluidic channels. *J. Colloid Interface Sci.* 357, 534–40.
- (49) Suter, S., and Skalak, R. (1993) The history of Poiseuille’s law. *Annu. Rev. Fluid Mech.*
- (50) Berthier, E., and Beebe, D. J. (2007) Flow rate analysis of a surface tension driven passive micropump. *Lab Chip* 7, 1475–8.
- (51) Roe, R. (1975) Wetting of fine wires and fibers by a liquid film. *J. Colloid Interface Sci.* 50, 0–9.
- (52) Lun, L. (2012) Development of Artificial Duck Feather Fibers.
- (53) Rumscheidt, F., and Mason, S. (1962) Break-up of stationary liquid threads. *J. Colloid Sci.* 269, 260–269.
- (54) Jin, B.-J., and Yoo, J. Y. (2011) Visualization of droplet merging in microchannels using micro-PIV. *Exp. Fluids* 52, 235–245.
- (55) Paik, P., Pamula, V. K., Pollack, M. G., and Fair, R. B. (2003) Electrowetting-based droplet mixers for microfluidic systems. *Lab Chip* 3, 28–33.

- (56) Lai, Y.-H., Hsu, M.-H., and Yang, J.-T. (2010) Enhanced mixing of droplets during coalescence on a surface with a wettability gradient. *Lab Chip* 10, 3149–56.
- (57) Lai, Y.-H., Yang, J.-T., and Shieh, D.-B. (2010) A microchip fabricated with a vapor-diffusion self-assembled-monolayer method to transport droplets across superhydrophobic to hydrophilic surfaces. *Lab Chip* 10, 499–504.
- (58) Konisho, T., and Ueno, I. (2009) Detection of advancing edge and length of precursor film ahead of macroscopic contact line of droplet spreading on solid substrate. *Ann. N. Y. Acad. Sci.* 1161, 292–303.
- (59) Hirose, K., Konisho, T., and Ueno, I. (2007) Existing length of precursor film on inclined solid substrate. *Microgravity Sci. Technol.* 19, 81–83.
- (60) Kavehpour, H., Ovryn, B., and McKinley, G. (2003) Microscopic and Macroscopic Structure of the Precursor Layer in Spreading Viscous Drops. *Phys. Rev. Lett.* 91, 196104.
- (61) Ueno, I., Hirose, K., Kizaki, Y., Kisara, Y., and Fukuhara, Y. (2012) Precursor Film Formation Process Ahead Macroscopic Contact Line of Spreading Droplet on Smooth Substrate. *J. Heat Transfer* 134, 051008.
- (62) Xu, H., Shirvanyants, D., Beers, K., Matyjaszewski, K., Rubinstein, M., and Sheiko, S. (2004) Molecular Motion in a Spreading Precursor Film. *Phys. Rev. Lett.* 93, 206103.
- (63) Popescu, M. N., Oshanin, G., Dietrich, S., and Cazabat, a-M. (2012) Precursor films in wetting phenomena. *J. Phys. Condens. Matter* 24, 243102.
- (64) Kizaki, Y., Konisho, T., and Ueno, I. (2007) Precursor film ahead droplet on solid with temperature gradient. *Microgravity Sci. Technol.* 19, 106–108.
- (65) Grest, G. S., Heine, D. R., and Webb, E. B. (2006) Liquid nanodroplets spreading on chemically patterned surfaces. *Langmuir* 22, 4745–9.
- (66) Huang, J. Y., Lo, Y.-C., Niu, J. J., Kushima, A., Qian, X., Zhong, L., Mao, S. X., and Li, J. (2013) Nanowire liquid pumps. *Nat. Nanotechnol.* 8, 277–281.
- (67) Mchale, G., Newton, M. I., and Carroll, B. J. (2001) The Shape and Stability of Small Liquid Drops on Fibers. *Oil Gas Sci. Technol.* 56, 47–54.
- (68) Carroll, B. . (1976) The accurate measurement of contact angle, phase contact areas, drop volume, and Laplace excess pressure in drop-on-fiber systems. *J. Colloid Interface Sci.* 57, 488–495.

APPENDICES

Appendix A

Derivation of Equation

The derivation below is trying to simulate the liquid motion along multifilament yarn. The start equation is based on Hagen Poiseuille Law. A fluid of constant density ρ and viscosity μ flows through a horizontal pipe of radius R and length L shown in figure below. The pressures at the centers of the inlet and exit are p_1 and p_2 , respectively. You may assume that the only nonzero velocity component is v_z , and that this not a function of the angular coordinate, θ .

$$Q = \frac{K_1}{\eta} \cdot \frac{P_1 - P_2}{L}$$

$$P_1 - P_2 = \Delta P_1 - \Delta P_2 = 2\gamma_{LV} \left(\frac{1}{R_1} - \frac{1}{R_2} \right) = 2\gamma_{LV} \left[\left(\frac{3V_1}{4\pi} \right)^{-1/3} - \left(\frac{3V_2}{4\pi} \right)^{-1/3} \right]$$

$$dx = Q dt$$

$$Q dt = \frac{2\gamma_{LV}K_1}{\eta L} \left[\left(\frac{3(V_1-x)}{4\pi} \right)^{-1/3} - \left(\frac{3(V_2+x)}{4\pi} \right)^{-1/3} \right] dt = dx$$

$$\frac{2\gamma_{LV}K_1}{\eta L} dt = \frac{1}{\left[\left(\frac{3(V_1-x)}{4\pi} \right)^{-1/3} - \left(\frac{3(V_2+x)}{4\pi} \right)^{-1/3} \right]} dx$$

$$\int_0^T \frac{2\gamma_{LV}K_1}{\eta L} dt = \int_0^{V_1} \frac{1}{\left[\left(\frac{3(V_1-x)}{4\pi} \right)^{-1/3} - \left(\frac{3(V_2+x)}{4\pi} \right)^{-1/3} \right]} dx$$

$$T = \frac{\sqrt[3]{3}\eta}{2(4\pi)^{1/3}\gamma_{LV}K_1} \int_0^{V_1} \frac{L}{[(V_1-x)^{-1/3} - (V_2+x)^{-1/3}]} dx$$

$$T = K \int_0^{V_1} \frac{L}{\left[(V_1 - x)^{-\frac{1}{3}} - (V_2 + x)^{-\frac{1}{3}} \right]} dx$$

$$T = K \frac{\eta L}{\gamma_{LV}} \int_0^{V_1} \frac{1}{\left[(V_1 - x)^{-\frac{1}{3}} - (V_2 + x)^{-\frac{1}{3}} \right]} dx = KY$$

Matlab code for transferring 'cine' files to videos and images

```
clear all;
clc;

Tosaveimages =1;

cm=colormap(gray); % color map uses 'jet'

n=size(num,1);
st=0;
InjDelay =0;
Fuel='diesel';O2='12%';T='8000K';

for j=1:n

% open the file
fid = fopen(filename, 'r');

% read the count of images saved to this file
f_pt = fseek(fid, 20, 'bof');
ImageCount = fread(fid, 1, 'uint32');

% read the image header offset
OffImageHeader = fread(fid, 1, 'uint32');

% read the image setup offset
OffSetup = fread(fid, 1, 'uint32');

% read the offset for the image
OffImageOffsets = fread(fid, 1, 'uint32');

% read the image width and height
```

```

f_pt = fseek(fid, OffImageHeader+4, 'bof');
biWidth = fread(fid, 1, 'int32');
biHeight = fread(fid,1, 'int32');

% read bit per pixel
f_pt = fseek(fid, 2, 'cof');
biBitCount = fread(fid, 1, 'uint16');
pxlbit = strcat('uint', int2str(biBitCount));

% read the frame rate
f_pt = fseek(fid, OffSetup, 'bof');
Framerate = fread(fid, 1, 'uint16');
FrameTime = 1/Framerate*1000; % unit: ms

% read the image pointer table
f_pt = fseek(fid, OffImageOffsets, 'bof');
pImag = fread(fid, ImageCount, 'uint32');

% read the images before fuel come out as background reference
f_pt = fseek(fid, pImag(1,1), 'bof');
pixels_0 = zeros(biWidth, biHeight);

%Upto this point is preparing to read a cine file
cinframesback = zeros(biWidth, biHeight);
ImageFrame=zeros(biWidth, biHeight);

FrameNumber=ImageCount;

filename_video = sprintf('D:\\matlabimage\\f\\f1\\videos');
filename_image = sprintf('D:\\matlabimage\\f\\f1\\images');

    for k=1:n
        %filename = sprintf('C:\\JW\\Chamber\\Experiment data\\1hole\\High
speed camera for liquid and
NL\\NL\\20130218_jetfuel\\images\\test%s',num(k,:));
        filename = sprintf('D:\\matlabimage\\f\\f1\\images%s', num(k,:));
        mkdir(filename);
    end
%
    stt=sprintf('test%s',num(j,:));
    outfile = fullfile(filename_video, strcat(stt, '.avi'));
filename = sprintf('D:\\matlabimage\\f\\f1\\videos');
    mkdir(filename);

```

```

aviobj=avifile(outfilename, 'compression', 'none', 'fps', 10);

for i=1:500
    i
    AnnotationSize = fread(fid, 1, 'uint32');
    Imagesize = fread(fid, 1, 'uint32');
    ImageFrame(:, :) = fread(fid, [biWidth, biHeight], pxlbit);
    if(rem(i,1)==0) % determin how many images are abstracted
        pixels=imrotate(ImageFrame,90);
        pixels=uint8(pixels);
        pixels=imadjust(pixels,[0.05 0.9],[,]); % [0.05 0.25] for image; [0.05
0.5] for movie
        bottomHeight = 1;
        imm=zeros(biHeight+bottomHeight,biWidth);
        imm(1:biHeight,:)=pixels(1:biHeight,:);
        imm=uint8(imm);
        %imm = imrotate(imm,-1.5,'bilinear','crop');
        pt=st*FrameTime+(i-1)*FrameTime-InjDelay; %% calculate the time shown

        imshow(imm, 'Border', 'tight');

        mov=getframe();
        %   ffm=gcf;
        if (Tosaveimages == 1)
            stime = strcat('1_', num2str(i));
            stt2=strcat(filename_image, num(j,:));
            outfilename = fullfile(stt2, strcat(stime, '.bmp'));
            %   imwrite(frame2im(getframe(gcf)),cm, outfilename, 'png');
            imwrite(frame2im(mov),cm, outfilename, 'bmp');
        end % to save imagesim2frame
        aviobj=addframe(aviobj,mov);
    end;
end;
fclose(fid);
aviobj=close(aviobj);

clear mov;
end;

```

Gibbs free energy of the microliter droplet on spindle knots